

Atomic force microscopy: Emerging illuminated and *operando* techniques for solar fuel research

Cite as: J. Chem. Phys. **153**, 020902 (2020); <https://doi.org/10.1063/5.0009858>

Submitted: 06 April 2020 . Accepted: 05 June 2020 . Published Online: 10 July 2020

Weilai Yu , Harold J. Fu , Thomas Mueller, Bruce S. Brunschwig , and Nathan S. Lewis 

COLLECTIONS

 This paper was selected as Featured



[View Online](#)



[Export Citation](#)



[CrossMark](#)

Lock-in Amplifiers
up to 600 MHz



Atomic force microscopy: Emerging illuminated and *operando* techniques for solar fuel research



Cite as: J. Chem. Phys. 153, 020902 (2020); doi: 10.1063/5.0009858

Submitted: 6 April 2020 • Accepted: 5 June 2020 •

Published Online: 10 July 2020



View Online



Export Citation



CrossMark

Weilai Yu,¹ Harold J. Fu,¹ Thomas Mueller,² Bruce S. Brunschwig,^{3,a)} and Nathan S. Lewis^{1,3,b)}

AFFILIATIONS

¹ Division of Chemistry and Chemical Engineering, California Institute of Technology, Pasadena, California 91125, USA

² Bruker Nano Surfaces, 112 Robin Hill Road, Santa Barbara, California 93111, USA

³ Beckman Institute, California Institute of Technology, Pasadena, California 91125, USA

^a) Author to whom correspondence should be addressed: bsb@caltech.edu

^b) Email: nsl Lewis@caltech.edu

ABSTRACT

Integrated photoelectrochemical devices rely on the synergy between components to efficiently generate sustainable fuels from sunlight. The micro- and/or nanoscale characteristics of the components and their interfaces often control critical processes of the device, such as charge-carrier generation, electron and ion transport, surface potentials, and electrocatalysis. Understanding the spatial properties and structure–property relationships of these components can provide insight into designing scalable and efficient solar fuel components and systems. These processes can be probed *ex situ* or *in situ* with nanometer-scale spatial resolution using emerging scanning-probe techniques based on atomic force microscopy (AFM). In this Perspective, we summarize recent developments of AFM-based techniques relevant to solar fuel research. We review recent progress in AFM for (1) steady-state and dynamic light-induced surface photovoltage measurements; (2) nanoelectrical conductive measurements to resolve charge-carrier heterogeneity and junction energetics; (3) *operando* investigations of morphological changes, as well as surface electrochemical potentials, currents, and photovoltages in liquids. Opportunities for research include: (1) control of ambient conditions for performing AFM measurements; (2) *in situ* visualization of corrosion and morphological evolution of electrodes; (3) *operando* AFM techniques to allow nanoscale mapping of local catalytic activities and photo-induced currents and potentials.

Published under license by AIP Publishing. <https://doi.org/10.1063/5.0009858>

I. INTRODUCTION

The photoelectrochemical (PEC) generation of fuels from sunlight is a promising approach to the production of sustainable, energy-dense chemical fuels without the net release of CO₂.¹ An integrated PEC solar fuel device consists of three major components: (1) semiconducting light-absorbers that generate separated electrons and holes; (2) catalysts that facilitate multi-electron transfer fuel-forming reactions; and (3) an ion-exchange membrane separating the anode and cathode compartments that contain the oxidized and reduced (i.e., fuel) products, respectively.^{2–5} To prevent pH changes, the membrane must also facilitate charge transport of protons or hydroxide ions between the two compartments.⁶ These components

often operate in highly acidic or alkaline electrolytes to minimize resistive losses, making the susceptibility of each component toward corrosion a key consideration in device design.^{7,8} Protective coatings can be used to prevent or mitigate semiconductor corrosion and as a secondary benefit, may allow tuning of the band-edge positions relative to the solution redox potentials.⁹

Micro- or nanoscale structuring of the semiconductors and/or catalysts allows control of several aspects of the device. The structure of the semiconductor, such as its mesoscale surface morphology, exposed facets, and the presence of grain boundaries, has a direct influence on properties such as charge mobility, light absorption, energetics, and processability.^{10,11} Structured semiconductors can be organized as micro- or nanowires embedded in an

ion-exchange membrane or can be dispersed in the solution as nanoparticles to obtain low electrolyte resistance and efficient light management.^{6,12–14} To optimize the surface area and minimize parasitic light absorption, the catalyst can also be structured in localized areas over the semiconductor into nanoparticles, nanowires, or ultra-thin coatings.^{15–17} The integration of these disparate components leads to further complexities at the interfaces. For example, on *n*-Si sparsely coated with Ni nanoparticles in contact with an electrolyte, the effective barrier height in the system is dominated by the higher barrier of the *n*-Si/electrolyte junction rather than that of the low-barrier *n*-Si/Ni junction.¹⁸

Atomic force microscopy (AFM) is a powerful characterization tool that can probe the properties of photoelectrodes with nanometer-scale resolution. First developed to map surface topography, the range of measurements has recently been expanded to include *in situ* conductivity, local electrochemical potential, surface photovoltage, and contact potential at the nanoscale, often in electrolyte and under operating conditions.^{19,20} Advanced AFM techniques have been used to better understand the properties of perovskites and organic photovoltaics, but have only recently been used on PEC materials.^{21–26}

The operation of AFM involves the raster scanning of a sharp tip over a sample surface (Fig. 1). Typically, the tip is attached to a cantilever whose deflection is detected by using a quadrant photodetector monitoring the light beam reflected off the top of the cantilever. Initially, scanning was accomplished in contact mode (CM) by simply dragging the tip across the surface. A feedback loop maintains a constant downward force on the tip while scanning is effected by driving a piezoelectric positioner oriented perpendicular to the surface. However, CM often damages the surface and/or the tip, so softer tapping modes were developed. In standard tapping mode (TM), the cantilever oscillates in resonance, whereas in PeakForce tapping (PFT), a sinusoidal drive is employed far off resonance.^{27–31} In both PFT and TM, the feedback loop controls the tip height above the surface. For TM, the feedback error signal is based on the oscillation amplitude, whereas PFT uses a synchronous measurement of the force at maximum extension. The method entails the use of fixed high (resonance) frequencies in TM (typically >50 kHz in air) vs more variable, lower frequencies in PFT (0.125 kHz–8 kHz). Regardless of the mode employed, a three-dimensional (3D) topographic map of the surface is produced.

While measuring the topography, the tip can also be used to measure additional mechanical and electrical properties at the nanometer-scale such as conductivity, electrostatic potential, and surface potential.

Conductive AFM (C-AFM) measures the DC conductivity between the sample and a conductive tip. The measurement requires physical contact between the surface and the tip, so CM has been traditionally used. However, soft samples such as organic photovoltaics or samples with loosely adsorbed particles are difficult to image in CM.³² Integration of C-AFM with TM is hindered by the short duty cycle during the contact of the tip with the surface. The high frequencies (typically >50 kHz) and Q-factors (~100) of TM conspire to produce sub- μ s contact times. In contrast, PFT's non-resonant tapping has contact times of ~0.1 ms, enabling conductivity measurements on soft and fragile samples.^{33–35} In addition, C-AFM offers the possibility of measuring the current–voltage behavior of the sample at every pixel, generating large multidimensional datasets.

AFM-based work-function measurements typically employ Kelvin Probe Force Microscopy (KPFM).³⁶ The AFM tip first scans across the surface topography and then scans back maintaining a constant height (typically 100 nm–200 nm), during which the surface and conductive tip form a capacitor. The electrostatic forces associated with capacitive charging serve as an error signal that adjusts an electrical bias applied between the tip and the surface to compensate the charging and, thereby, measure the contact potential difference (CPD) or work-function difference between the tip and the sample. Results are calibrated using samples with a well-defined, known work function.

Both C-AFM and KPFM are traditionally performed in air. However, operation of solar fuel devices requires the presence of an electrolyte, and the semiconductor/catalyst interfaces are likely to change *in situ* under operation.^{37,38} KPFM suffers from electrical screening when employed in normal electrolytes, making it impractical for use in *operando* solar fuel studies. Measurements under operating conditions using C-AFM necessitate the use of an insulated nanoelectrode with only the end of the tip exposed to allow electrical contact with the surface.³⁹ The rest of the tip is insulated to minimize background currents from parasitic electrochemical reactions. Such probes have recently become available with an exposed Pt tip apex of ~50 nm diameter and ~200 nm length, where the

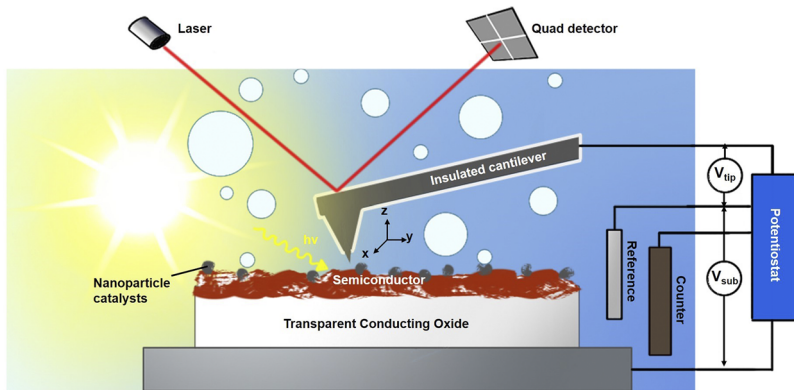


FIG. 1. Schematic illustration of a four-probe *operando* electrochemical AFM set up in liquid, showing an insulated AFM cantilever, the red position laser and quad detector used to detect the oscillations of the cantilever, potentiostatic control of the cantilever tip, and the back of the semiconductor substrate relative to the same reference electrode. The semiconductor is illuminated from its front side and covered with a nanoparticle catalyst.

rest of the tip is insulated with SiO_2 .⁴⁰ As shown in Fig. 1, this nanoelectrode probe can be used in a four-electrode electrochemical AFM (EC-AFM) cell, in which both the sample and tip are independent working electrodes, with common counter and reference (or quasi-reference) electrodes. In a conventional three-electrode EC-AFM setup, the tip spectates topography changes occurring during electrolysis. Using the probe as an active fourth electrode enables AFM-based scanning electrochemical microscopy (SECM), allowing mapping of the local electrochemical activity with sub-100 nm resolution. Moreover, use of the peakforce SECM probe as the fourth electrode allows sensing the local electrochemical potential on the electrode surface.^{38,41,42}

In this Perspective, we summarize recent developments of these emerging scanning-probe techniques for studying photoelectrodes in solar fuel devices. We focus on the following aspects: (1) light-illumination configurations integrated with AFM systems; (2) light-induced KPFM measurements of semiconductors in air to give spatially resolved measurements of surface photovoltages (SPVs); (3) spatially resolving the charge-carrier characteristics upon light excitation and junction energetics based on C-AFM in air; (4) liquid AFM measurements of morphological changes and electrical/potential signals of semiconductors/catalysts operating in electrolytes.

II. RECENT PROGRESS

A. AFM-based illumination setups for studying photoactive samples

Studying the photoactivity of materials with AFM requires illumination of the sample. One approach involves using the built-in laser, because light not reflected from the cantilever can generate charge carriers at the sample (Si) surface. However due to the shadowing of the cantilever, the sample area under the AFM tip is not directly illuminated. Laskowski *et al.* employed this method on an *n*-Si/Ni photoanode in an electrolyte, yielding open-circuit potential (OCP) values comparable to those from macroscopic PEC measurements.³⁸

External front-side illumination using fiber optics can provide direct illumination to the local area being probed, but given the close proximity of the probe to the sample, the incident light must enter at an angle of $<20^\circ$ to the horizontal to avoid shadowing. Alternatively, the sample can be illuminated from the back-side when mounted on a transparent stage, but carrier generation near the semiconductor surface is reduced due to light absorption through the bulk of the semiconductor.²³ Semiconductors with minority-carrier diffusion lengths shorter than the sample thickness would consequently have less carrier collection at the AFM tip.

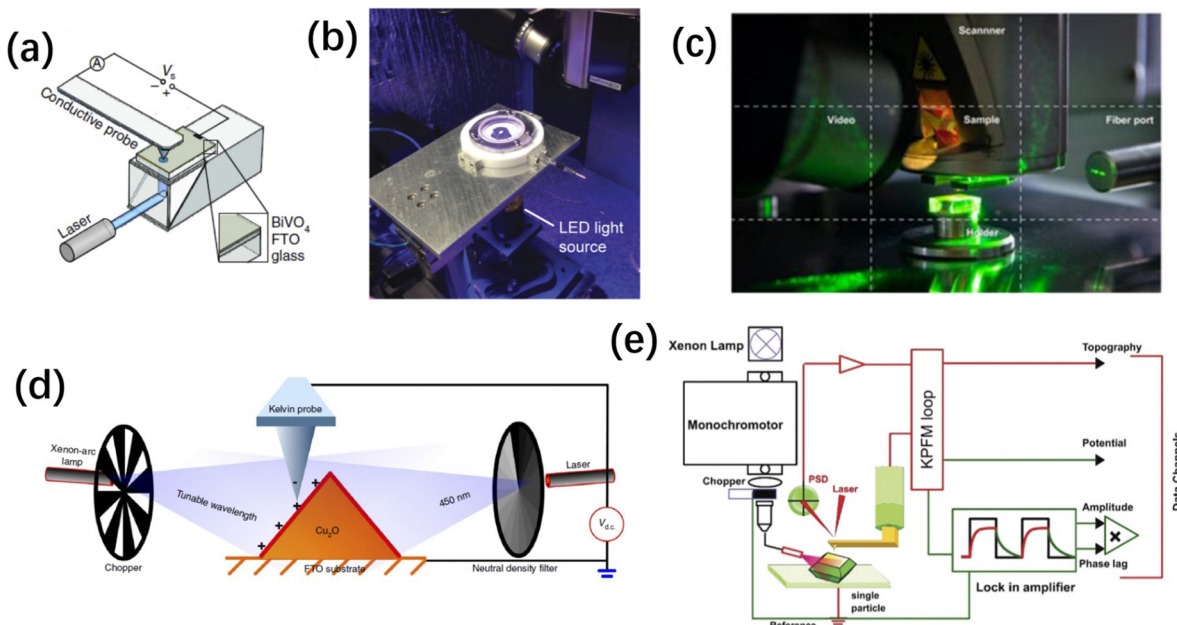


FIG. 2. Summary of typical optical setups for illuminated AFM-based measurements. (a) Schematic diagram of the back-side illumination setup with an underlying mirror tilted at $\sim 45^\circ$.⁴³ (b) optical image of a direct back-side illumination setup using an LED light source beneath samples immersed in an EC cell.⁴¹ (c) optical image of a direct front-side illumination setup by a single light beam with a fiber-optic port; (d) schematic diagram of front-side illumination by a dual-beam setup.^{44,45} (e) schematic illustration of the integration of the AFM system with the associated optical and electrical components in (c) and (d), allowing simultaneous coupling and collection of electrical/optical signals.^{10,44} (a) is reproduced with permission from Eichhorn *et al.*, “Nanoscale imaging of charge carrier transport in water splitting photoanodes,” Nat. Commun. **9**(1), 2597 (2018). Copyright 2018 Author(s), licensed under a Creative Commons Attribution 4.0 License; (b) is reproduced with permission from Nellist *et al.*, “Potential-sensing electrochemical atomic force microscopy for *in operando* analysis of water-splitting catalysts and interfaces,” Nat. Energy **3**(1), 46–52 (2017). Copyright 2017 Nature Publishing Group; (c) and (e) are reproduced with permission from Chen *et al.*, “Imaging photogenerated charge carriers on surfaces and interfaces of photocatalysts with surface photovoltaic microscopy,” Chem. Soc. Rev. **47**(22), 8238–8262 (2018). Copyright 2018 Royal Society of Chemistry; and (d) is reproduced with permission from Chen *et al.*, “Charge separation via asymmetric illumination in photocatalytic Cu_2O particles,” Nat. Energy **3**(8), 655–663 (2018). Copyright 2018 Nature Publishing Group.

Several recently reported optical AFM-based setups are summarized in Fig. 2. Figure 2(a) displays a back-side illumination scheme employed by Eichhorn *et al.*⁴³ The sample is deposited on a transparent fluorine-doped tin oxide (FTO)-coated glass substrate and illuminated by using an external cw-diode laser reflected by a 45° mirror underneath the sample. With this arrangement, the light source can be positioned remotely from the sample stage. If enough space is available between the AFM controller and the sample stage, a light source can be placed directly beneath the AFM sample [Fig. 2(b)].⁴¹ In contrast, a front-side illumination setup is shown in Fig. 2(c), in which the light beam enters at a small angle to the horizontal to avoid shadowing of the cantilever.¹⁰ Two independent light sources from different directions [Fig. 2(d)] have also been used to produce illuminated/shadow facets on a single Cu₂O particle.⁴⁵ In all of these optical AFM setups, the light-induced responses (surface photovoltage, etc.) can be studied on a nanometer scale at specific surface features, as functions of the wavelength and intensity of the light.^{46,47} The use of an optical chopper allows investigation

of the dynamic surface response by contrasting the temporal response of the electrical signal between light and dark conditions. The chopped optical signals monitored using a lock-in amplifier need to be synchronized with the AFM operation [Fig. 2(e)].¹⁰

B. Surface photovoltage measurement of semiconductors to probe charge separation

KPFM can measure the contact potential difference (CPD) between the tip and the sample.³⁶ Zhu *et al.* integrated KPFM with an illumination source to measure the surface photovoltage (difference in CPD under illumination and in the dark) and, thus, performed spatially resolved surface photovoltage spectroscopy (SR-SPS).¹⁰ This technique has proven to be a powerful tool for measuring the light/dark differences under steady-state or dynamic conditions for a variety of semiconductors including BiVO₄, TiO₂, Cu₂O, etc.^{10,45,48,49} The change in the work function upon light excitation can indicate the doping type (*n*- or *p*-type) of the

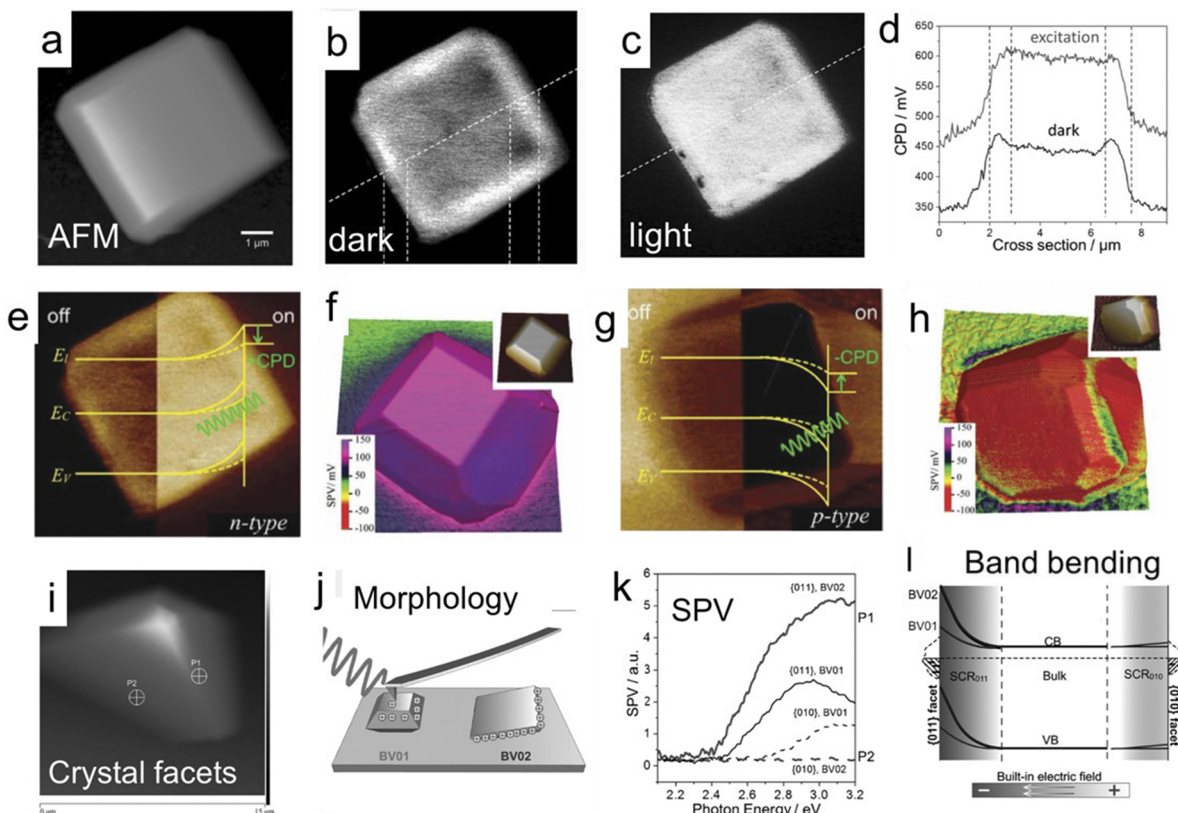


FIG. 3. SR-SPS reveals differences in light and dark of semiconductor materials under steady-state conditions. (a) AFM topographic image; [(b) and (c)] KPFM images under dark and light for a single BiVO₄ particle; (d) comparison of the measured CPD values from (b) to (c) across the crystal facets;¹⁰ [(e)–(h)] comparisons of dark and light KPFM images and SPV mappings for [(e) and (f)] *n*-type BiVO₄; [(g) and (h)] *p*-type Cu₂O;⁴⁹ [(i)–(l)] SR-SPS reveals the effects of (i) different crystal facets,¹⁰ [(j) and (k)] morphology of BiVO₄ toward the SPV signals,¹⁰ and (l) the underlying band bending within the depletion region at different facets on a single BiVO₄ crystal.¹⁰ (a)–(d) and (i)–(k) are reproduced with permission from Zhu *et al.*, “Direct imaging of highly anisotropic photogenerated charge separations on different facets of a single BiVO₄ photocatalyst,” *Angew. Chem., Int. Ed.* **54**(31), 9111–9114 (2015). Copyright 2015 Wiley-VCH Verlag GmbH & Co. (e)–(h) are reproduced with permission from Chen *et al.*, “Unravelling charge separation via surface built-in electric fields within single particulate photocatalysts,” *Faraday Discuss.* **198**, 473–479 (2017). Copyright 2017 Royal Society of Chemistry.

semiconductor. The effects of different crystal facets, crystal defects, phase junctions, and co-catalysts on charge separation have been studied by this technique. Furthermore, probing the surface charge accumulation and band bending within the depletion region provides insight into the charge separation mechanism in semiconductor photocatalysts under illumination.

SR-SPS was initially applied to a model system involving BiVO_4 semiconductor crystals with well-defined facets [Figs. 3(a)–3(d)].¹⁰ The dark and light KPFM images were overlaid at each pixel to yield a spatially resolved SPV map, which was then correlated with the sample surface topography. Upon illumination, the CPD of *n*- BiVO_4 and *p*- Cu_2O crystals increased and then decreased, resulting in positive and negative SPV signals, respectively [Figs. 3(e)–3(h)].⁴⁹ The positive and negative signs of the SPV signals indicated the accumulation of photogenerated holes or electrons, respectively, at the surface under light excitation. In general, a larger SPV signal suggests enhanced charge separation and accumulation at the

semiconductor surface as well as increased band bending in the depletion region.

With a well-defined crystal morphology, the SPV signals can be quantitatively compared for different facets to reveal crystal anisotropy [Figs. 3(i) and 3(j)]. Different crystal facets of BiVO_4 display different CPDs in the dark as well as different SPV signals under illumination. By tuning the wavelength of the light, the SPV signals can be studied as functions of photon energy. Large increases in SPVs were observed when the photon energies were above the bandgap of BiVO_4 [Fig. 3(k)].¹⁰ Moreover, the (011) facets of BiVO_4 exhibited larger SPV responses than those observed from the (010) facets; furthermore, the overall morphology of the BiVO_4 crystal also influenced the SPV signal. This behavior suggests that the band bending and driving force of charge separation at one crystal facet are influenced by the properties of the other facets on the same crystal. By optimizing the ratio between different facets on a crystal, asymmetric band bending can be realized to enable more efficient

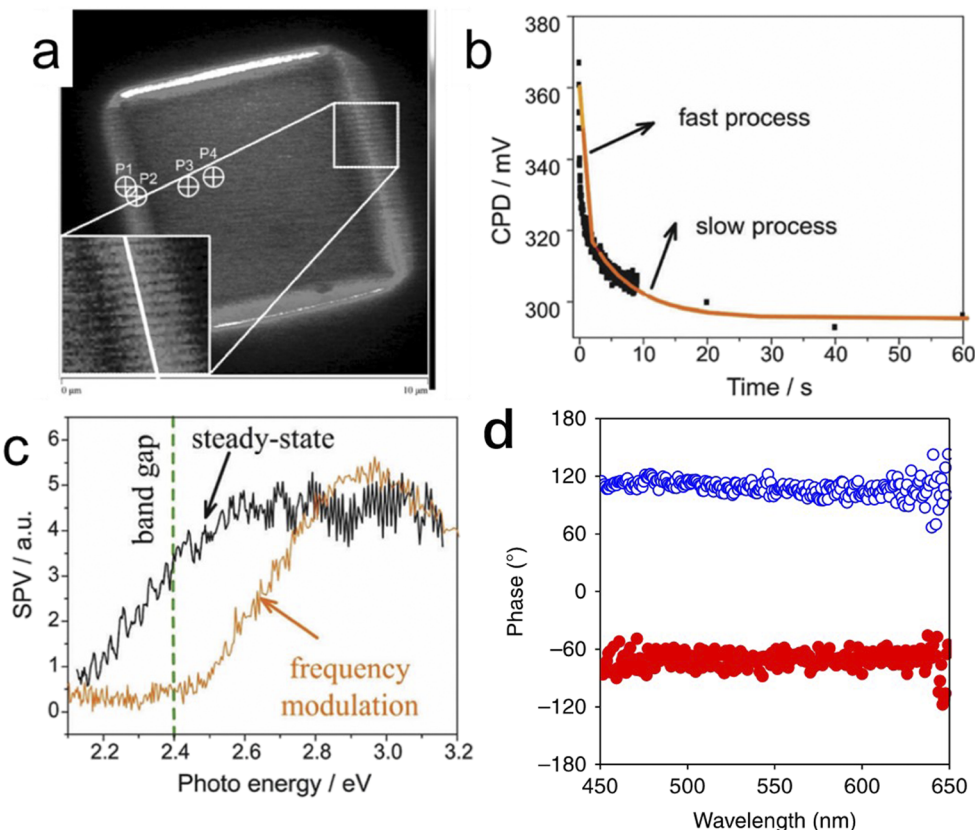


FIG. 4. [(a)–(c)] Dynamic charge-carrier behavior of BiVO_4 .¹⁰ (a) Frequency-modulated SPV mapping of the BiVO_4 crystal under chopped illumination; (b) decay of the CPD signal vs time displaying both fast and slow processes; (c) comparison of SPV signals under steady-state and 10 Hz frequency-modulated illumination as a function of photon energy.^{10,44} (d) the phase values of SPVs under 5 Hz-modulated excitation for the illuminated (blue) and shadowed facet over a single Cu_2O particle.⁴⁵ (a) is reproduced with permission from Zhu *et al.*, "Direct imaging of highly anisotropic photogenerated charge separations on different facets of a single BiVO_4 photocatalyst," *Angew. Chem., Int. Ed.* **54**(31), 9111–9114 (2015). Copyright 2015 Wiley-VCH Verlag GmbH & Co. (b) and (c) are reproduced with permission from Chen *et al.*, "Imaging photogenerated charge carriers on surfaces and interfaces of photocatalysts with surface photovoltage microscopy," *Chem. Soc. Rev.* **47**(22), 8238–8262 (2018). Copyright 2018 Royal Society of Chemistry; (d) is reproduced with permission from Chen *et al.*, "Charge separation via asymmetric illumination in photocatalytic Cu_2O particles," *Nat. Energy* **3**(8), 655–663 (2018). Copyright 2018 Nature Publishing Group.

charge separation [Fig. 3(l)].¹⁰ More recently, the facet dependence of the SPV signals has been attributed to the different charge-carrier mobilities along different crystallographic orientations.⁵⁰

The SR-SPS technique was used to probe transient carrier dynamics of semiconductors such as BiVO₄ and Cu₂O (Fig. 4). Under 10 Hz chopped illumination at 395 nm, highly contrasting stripes were observed in the KPFM image of BiVO₄. The stripes are due to the changes in contact potential with the chopped illumination. The contrast was more intense on the (011) face of the crystal, illustrating the anisotropic nature of the charge separation on the BiVO₄ [Fig. 4(a)].¹⁰ The decay of its CPD signal with time after a light pulse consisted of fast (\leq s) and slow (\geq min) components [Fig. 4(b)].⁴⁴ By use of frequency-modulated chopped illumination, the fast component was observed to be independent of the slow component. The SPV signals of BiVO₄ under steady-state and 10 Hz illumination differed as functions of photon energy [Fig. 4(c)], with the phase of the lock-in amplifier providing the sign of the SPV and distinguishing between electron- and hole-rich facets. Under 5 Hz illumination, the phase values for the illuminated and shadowed facets of Cu₂O differed by 180° [Fig. 4(d)], indicating charge separation on the facets. The illuminated and shadowed facets were hole- and electron-rich, respectively.⁴⁵

In addition to single semiconductor particles, SR-SPS has been applied to more complicated systems to reveal their underlying mechanisms of charge separation:

1. Phase junction

A pure rutile TiO₂ nanorod (NR) phase was compared to a mixed phase of anatase nanoparticles (NP) deposited on the top

of rutile NRs. In the dark, the rutile TiO₂ was shown by KPFM to have a larger work function of ~30 mV than that of the anatase TiO₂.⁴⁸ At an anatase/rutile phase boundary, this difference in work function would give rise to a built-in electric field. Under illumination, the amplitude of the SPV increased dramatically at the boundary between the pure rutile phase and the mixed anatase/rutile phase. This increase showed that the rutile/anatase material had an improved charge separation compared to pure rutile. Furthermore, the phase of the frequency-modulated SPV shifted from $\sim +150^\circ$ (hole-rich at the surface) for the pure rutile to -50° (electron-rich) for the anatase/rutile mixed phase.⁴⁸ This behavior showed that the electric field formed at the anatase/rutile boundary due to the work-function difference affected transport of photogenerated electrons from the rutile to the anatase phase under UV light excitation.

2. Co-catalysts

The traditional role of a catalyst is to lower the kinetic barrier of the desired reaction. However, on semiconductors, deposited catalyst material can also influence the charge separation. SR-SPS is a powerful tool for resolving long-standing questions about the role of co-catalysts in photocatalysis.⁵¹ For BiVO₄, the selective deposition of MnO_x on the BiVO₄ (011) facet substantially increased the SPV signals (~+65 mV) relative to the behavior of the bare surface (~+7 mV) [Figs. 5(a) and 5(b)]. Furthermore, in the presence of MnO_x, the SPV signal on the (010) BiVO₄ facet had the opposite sign of ~ -35 mV, vs $\sim +3$ mV for the bare surface. This behavior indicates that after catalyst deposition, the (011) and (010) facets accumulate holes and electrons under illumination, respectively. The charge

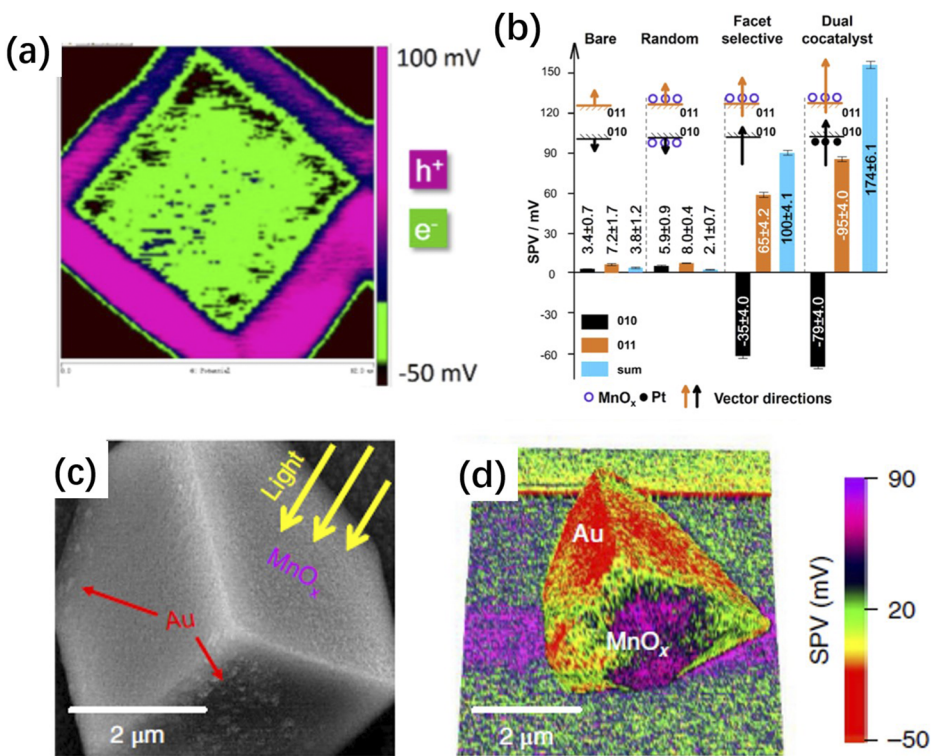


FIG. 5. (a) SPV imaging of the BiVO₄ crystal with selectively deposited catalysts (Pt and MnO_x); (b) quantitative comparisons of the SPV signals on different BiVO₄ facets before and after catalyst depositions under varied conditions;⁵¹ (c) SEM image of the Au and MnO_x selectively deposited over the Cu₂O crystal by asymmetric illumination; (d) its corresponding SPV mapping.⁴⁵ (a) and (b) are reproduced with permission from Zhu *et al.*, “Visualizing the nano cocatalyst aligned electric fields on single photocatalyst particles,” *Nano Lett.* **17**(11), 6735–6741 (2017). Copyright 2017 American Chemical Society; (c) and (d) are reproduced with permission from Chen *et al.*, “Charge separation via asymmetric illumination in photocatalytic Cu₂O particles,” *Nat. Energy* **3**(8), 655–663 (2018). Copyright 2018 Nature Publishing Group.

separation is highly directional due to the presence of the MnO_x catalyst on specific facets. Furthermore, selective deposition of Pt on the (010) facet with MnO_x on the (011) facet further increased the SPV differences between the two facets to ~ 174 mV, compared to the behavior with only MnO_x on the (011) facet of ~ 100 mV. These results show the significance of strategic placement of co-catalysts over semiconductors to optimize the charge separation efficiency and photocatalytic activities.⁵¹

3. Photo-Dember effect under asymmetric illumination

In contrast to the anisotropic BiVO_4 crystal, the cubic Cu_2O crystal displays isotropic facets that are expected to produce mutually similar band bending under homogeneous illumination. However, under asymmetric illumination, positive and negative SPV signals were observed at the illuminated and shadowed facets of Cu_2O , respectively.⁴⁵ This behavior implies accumulation of holes at illuminated facets and electrons at shadowed facets, leading to directional electron-hole separation in response to such asymmetric illumination. In response to tuning the Cu_2O crystal size, the substantially different SPV signals under dark and light can be ascribed quantitatively to the different mobilities of electrons and holes, known as the Photo-Dember effect.⁵² More importantly, this Photo-Dember effect can be applied to selectively deposit Au and MnO_x catalysts at the shadowed and illuminated areas, respectively, of the same Cu_2O crystal, to optimize the driving force of charge separation and photocatalytic activity [Figs. 5(c) and 5(d)].

4. Effect of surface defects

Electrodeposited Cu_2O crystals were used to study the effects of surface defects on charge separation.⁵³ The density of hole (Cu^{2+}) vs electron (Cu^0) trap sites in the Cu_2O was controlled by tuning the electrodeposition conditions. The SPV response showed that samples with more hole trap sites had a larger concentration of electrons at the surface and a negative SPV signal. Increasing the electron trap sites and decreasing the hole trap sites yielded more holes at the surface and resulted in a positive SPV signal. SR-SPS, moreover, showed that the SPV signal was reduced in the area where the AFM tip mechanically scratched away the surface and that the electron trap sites were located within 100 nm of the surface.⁵³

C. Nanoelectrical investigations of semiconductor, catalyst, and protective layers

C-AFM allows correlation between the morphology and the (photo)current response of PEC devices. Statistical analysis of features of polycrystalline semiconductors, such as grain boundaries and facet planes, can provide insight into the charge-transfer characteristics.^{11,43} The AFM tip can incorporate a variety of different conductive materials including Au, Pt, and Pt/Si, as well as diamond, so properties including the work function and tip geometry can affect the semiconductor/tip interface. The energetics at these interfaces can be further elucidated by the formation of ohmic or Schottky contacts with varying barrier heights.⁴³ C-AFM can also probe buried interfaces such as the semiconductor/catalyst junction, which can form high barrier-height heterojunctions or low resistance ohmic contacts.^{32,38,54} C-AFM can, moreover, probe for defects and define energetics of protective coatings that protect semiconductors from

dissolution in a corrosive electrolyte.⁵⁵ The following subsections summarize the use of C-AFM as categorized by the component and its associated interface.

1. Semiconductors

Electrodes can in principle be optimized through improved understanding of the heterogeneity of charge transfer in polycrystalline and nanostructured semiconductors. For example, grain boundaries often limit the performance by reducing conductivity or acting as charge recombination sites.^{43,56} C-AFM has been used to correlate the conductivity of hematite ($\alpha\text{-Fe}_2\text{O}_3$) with its structure when samples are grown under mutually different conditions.¹¹ For example, when samples were synthesized by vapor-phase deposition with temperatures and air-flow rates of either 475 °C at 2 L min⁻¹ or 545 °C at 6 L min⁻¹, higher temperatures and flow rates yielded larger nanoparticle aggregates with higher conductivity and fewer high-angle grain boundaries, resulting in reduced barriers to transport of majority carriers [Figs. 6(a), 6(b), 6(d), and 6(e)]. The improvement in electrical conductivity was quantified by analyzing the fractional area of the AFM map above a defined current threshold relative to the maximum current (I_{\max}) at different applied voltages [Figs. 6(c) and 6(f)]. Defining the threshold as $I_{\max}/10$ to account for variations in mobility related to crystal orientation, the data in Figs. 6(c) and 6(f) show that 99% of the current for samples synthesized using the 2 L min⁻¹ flow rate was below this threshold vs 61% for samples synthesized using the 6 L min⁻¹ flow rate. The amount of area exhibiting currents below the threshold correlated with the observed number of grain boundaries, supporting the hypothesis that carrier transport is limited through the high-angled grain boundaries.

The photocurrent-generation characteristics of semiconductors can be probed by illuminating the photoelectrode surface during the AFM scan and by applying a bias between the tip and the sample while measuring the current. As shown in Fig. 7, a recent study by Eichhorn *et al.* revealed the optoelectronic heterogeneity in BiVO_4 photoanodes.⁴³ Illuminating through the FTO back contact, the photogenerated charge carriers are collected at the front surface of BiVO_4 through the conductive AFM probe [Fig. 2(a)].

Photocurrents were measured using either a Pt/Ir- or an Au-coated probe at a reverse bias of 1.75 V. The measured photocurrents were plotted as a normalized histogram for grain boundaries, plane facets, and facet boundaries [Figs. 7(e) and 7(f)]. Formation of a contact with the Pt/Ir probe produced higher average photocurrents (1.31 pA) on facet boundaries compared to those on the facet plane (0.51 pA) and grain boundary (0.43 pA), whereas for contact with an Au probe, the facet boundary, facet plane, and grain boundary had relatively mutually similar average photocurrents of 1.06 pA, 0.95 pA, and 0.75 pA, respectively.⁴³

The current maps depend on the applied potential as well as the geometry and composition of the probe, which affects the contact area and the band alignment at the interface. The current observed depends on the balance of the interfacial energetics and the tip-sample contact area. In a nanoscale Schottky contact in reverse bias, a smaller radius is expected to have a shorter depletion width and leads to increased tunneling and higher current.⁵⁷ This dependence is opposite to that expected for contact area, for which a larger contact will increase the observed current. The expected contact area depends on the tip radius, the elastic moduli of the tip and

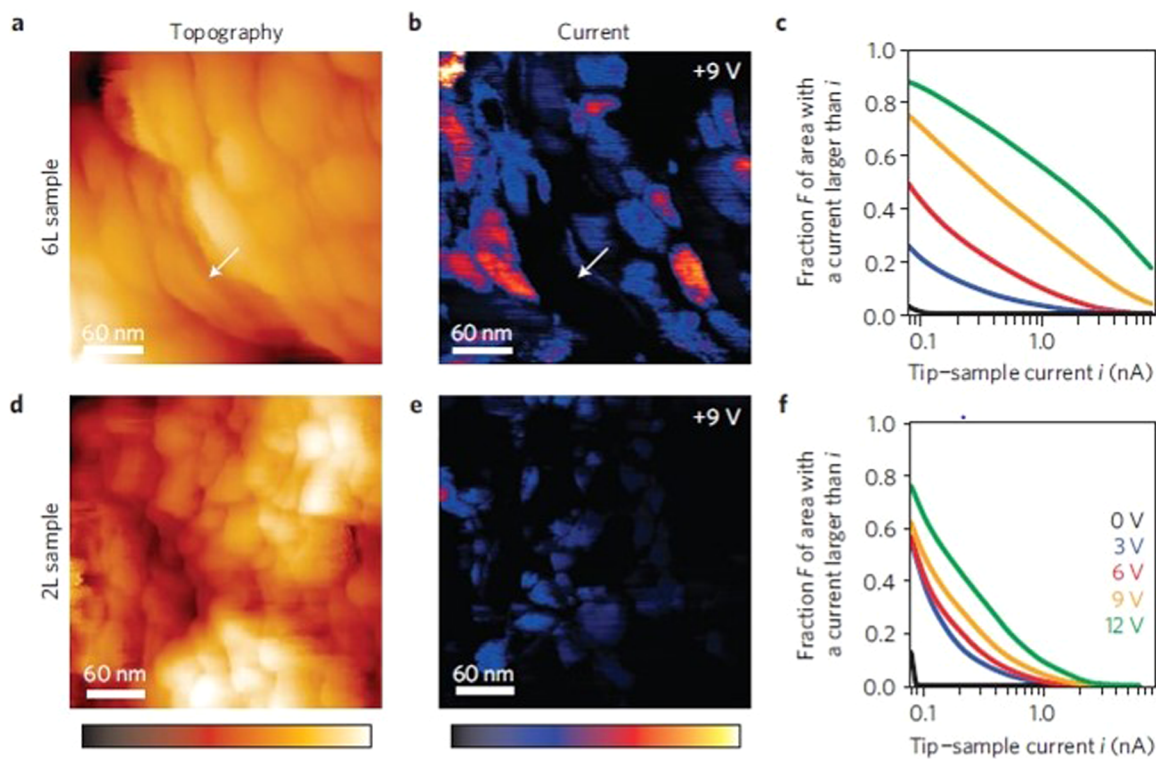


FIG. 6. C-AFM of α -Fe₂O₃. Electrodes prepared [(a)–(c)] at 545 °C flowing air at 6 L min⁻¹ and [(d)–(f)] at 475 °C at 2 L min⁻¹. [(a) and (d)] Topography measurements are shown with the scale representing a height variation of 140 nm; [(b) and (e)] current maps with the scale representing a current variation of 0 nA–5 nA. [(c) and (f)] Statistical distribution of the current maps at various applied voltages.¹¹ Reproduced with permission from Warren *et al.*, “Identifying champion nanostructures for solar water-splitting,” Nat. Mater. **12**(9), 842–849 (2013). Copyright 2013 Nature Publishing Group.

substrate, and the applied force. Use of a continuum mechanical model for stiff materials with a small tip radius yields estimates of the contact areas for the Pt/Ir- and Au-coated tips of 28 nm² and 8 nm², respectively.⁵⁸ The generally higher current observed for Au-coated probes suggests that the observed current was dominated by the nanoscale interface rather than by the contact area. The authors suggested that the mutually similar photocurrents from the Au probe could be due to the formation of a Schottky barrier that is ~0.1 eV lower than that for Pt/Ir.⁴³ Nonetheless, the mutually similar photocurrents at grain boundaries and facet planes for a given probe material suggest that the grain boundaries in BiVO₄ do not act as recombination sites. These findings underscore the interfacial defect tolerance of BiVO₄, yielding an advantage over the grain boundary-limited α -Fe₂O₃ in fabrication of a scalable and efficient photoanode.⁴³

2. Catalysts and semiconductor/catalyst interfaces

Multi-component catalyst coatings of (NiFeCoCe)_x on BiVO₄ photoanodes were designed by correlating macroscale PEC measurements with photoconductive AFM (PC-AFM).⁵⁴ NiO_x and FeO_x were used as catalysts, whereas CeO_x and CoO_x were used to modify the interfacial properties of the BiVO₄. The CeO_x passivated

electronically active trap states, improving the collection of photogenerated holes from the BiVO₄, whereas CoO_x lowered the interfacial energetics to allow an ohmic contact. A (CoFeCe)_x layer on BiVO₄ was, subsequently, designed to capture photogenerated holes from BiVO₄ and transport the holes to a catalytically active (NiFe)_x overlayer. Figure 8 shows comparisons of PC-AFM images of Ni_{0.8}Fe_{0.2}O_x, Co_{0.4}Fe_{0.1}Ce_{0.5}O_x, and Co_{0.4}Fe_{0.1}Ce_{0.5}O_x/Ni_{0.8}Fe_{0.2}O_y layers on BiVO₄, which demonstrate that the current increased on the top of the grains and not at grain boundaries. Additionally, the median photocurrents were substantially higher on the Co_{0.4}Fe_{0.1}Ce_{0.5}O_x/Ni_{0.8}Fe_{0.2}O_y layer, and the (CoFeCe)_x acted as a hole collection layer enhancing the current collected from Ni_{0.8}Fe_{0.2}O_x when Co_{0.4}Fe_{0.1}Ce_{0.5}O_x was inserted between Ni_{0.8}Fe_{0.2}O_x and BiVO₄.

Nanostructured catalyst designs can increase the surface area of the catalyst while minimizing the area that obscures the surface of the semiconductor. Discontinuous films of catalyst nanoparticles lower parasitic absorption by the opaque catalyst. Jiang *et al.* investigated electrolessly deposited Pt nanoparticles on *p*-Si to understand macroscale differences relative to electron-beam evaporated Pt on *p*-Si for the hydrogen evolution reaction.³² The Pt/*p*-Si contact was ohmic for evaporated Pt on *p*-Si due to the high work function of Pt, but C-AFM showed that individual electroless Pt nanoparticles

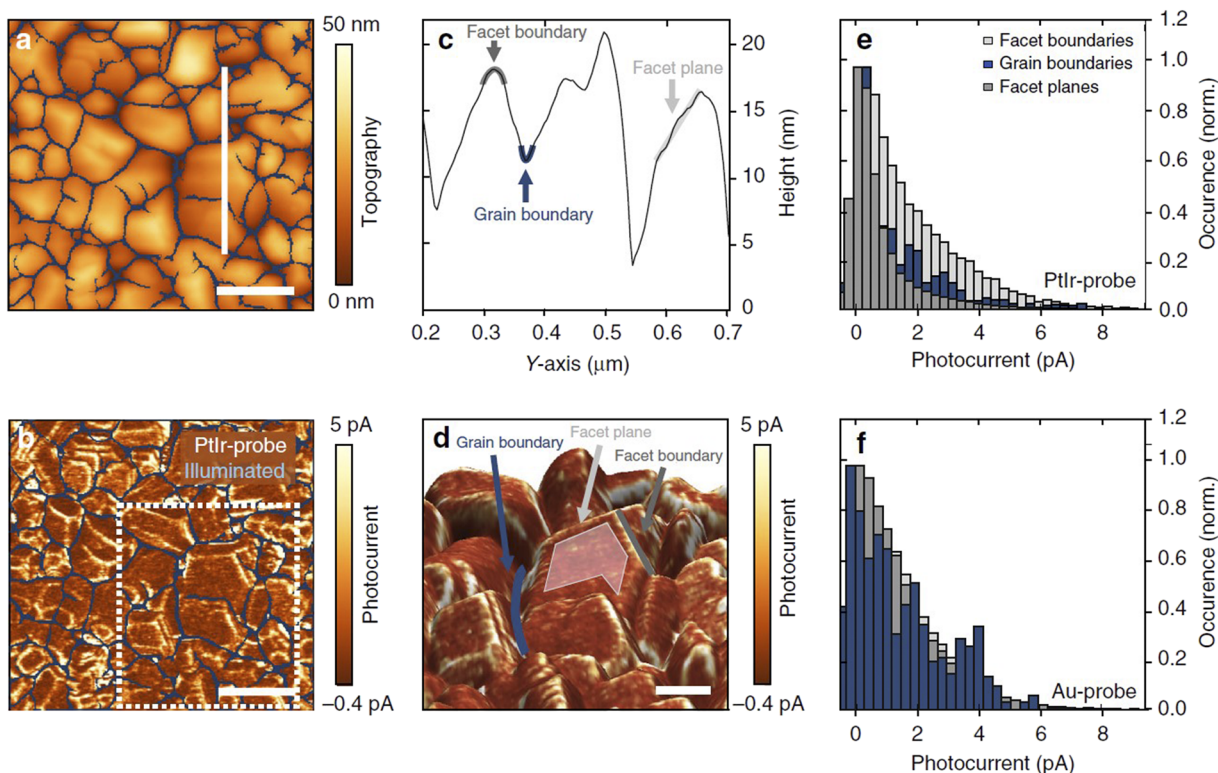


FIG. 7. Statistical analysis of BiVO₄ photocurrent distributions. (a) Topography and (b) photocurrent maps at 1.75 V using a Pt/Ir-coated tip with grain boundaries emphasized in blue. Scale bar: 200 nm. (c) Height profile along the white line in (a), and (d) photocurrent overlaid on the 3D-topography. (e) Representative grain boundary, facet boundary, and facet plane are illustrated. [(e) and (f)] Histograms of photocurrent distributions for (e) Pt/Ir- and (f) Au-coated probes.⁴³ Reproduced with permission from Eichhorn *et al.*, “Nanoscale imaging of charge carrier transport in water splitting photoanodes,” Nat. Commun. **9**(1), 2597 (2018). Copyright 2018 Author(s), licensed under a Creative Commons Attribution 4.0 License.

when deposited on *p*-Si exhibited rectifying behavior with a high resistance interface. Furthermore, only about a third of the particles had appreciable contact currents, with a 10³ difference observed in the contact currents of different particles (Fig. 9). X-ray photoelectron spectroscopy showed the formation of insulating SiO_x under the electrolessly deposited Pt.⁵⁹ The differences in behavior were consistently attributed to an insulating junction between the Si and Pt. Furthermore, the adhesion of nanoparticles was evaluated both in air and under electrolyte by using AFM probes with varying spring constants to push individual particles with a controlled force. Although the particles were mechanically well attached in air, they adhered only weakly in aqueous electrolyte.

A study by Zeradjanin *et al.* utilized C-AFM to understand how cracks in a RuO₂ catalyst layer affected its activity as an oxygen evolution reaction (OER) catalyst.⁶⁰ Both “cracked” and “crack-free” electrodes were synthesized using a sol-gel procedure. Varying the concentration of the sol solution and the number of coating-drying-sintering cycles allowed control of the morphology. Samples with cracks of ~10 μm width were observed with higher conductivity at the edges of terraces, whereas conductive spots were more randomly distributed in crack-free samples. These conductive spots indicated areas that supported high local current densities and, consequently, where activity was concentrated. In addition to the increased active

surface area of the cracked samples, the cracks facilitated limited growth and detachment of evolved gas bubbles and, consequently, increased the activity of the catalyst.⁶⁰

3. Protective coatings

Coatings of a metal oxide have been used to protect electrodes for extended periods of time under oxidizing conditions, but the failure modes of protective coatings are not well understood.⁹ These protective layers must allow electrons or holes to pass while being impermeable to the electrolyte. Amorphous TiO₂ conducts holes for photoanodes in 1.0M KOH via Ti³⁺ defect states and, consequently, allows for effective catalysis of the OER on a metallized surface.^{61,62} In one instance, C-AFM was used to identify that a conductive metastable phase existed within the amorphous TiO₂ protective layer on Si.⁵⁵ The surface contained conductive spots that were correlated with the non-bulk crystalline phases as determined by convergent-beam electron spectroscopy. Pinhole formation was observed at these crystalline sites after operation. The pinholes, subsequently, allowed the electrolyte to penetrate and corrode the underlying Si. Reducing the TiO₂ film thickness suppressed the nucleation of these crystalline phases and, subsequently, extended the operational lifetime of the electrode to more than 500 h.

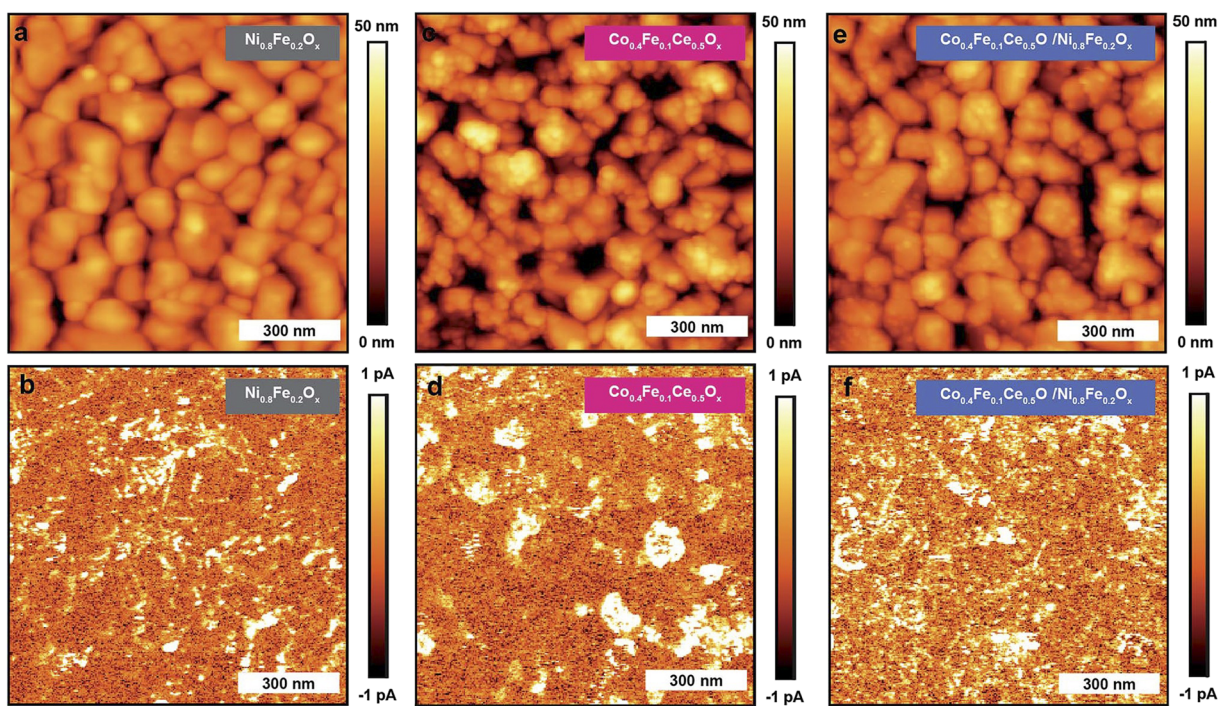


FIG. 8. PC-AFM measurements of BiVO_4 /catalyst interfaces. [(a), (c), and (d)] Topographic and [(b), (d), and (f)] current maps of [(a) and (b)] $\text{BiVO}_4/\text{Ni}_{0.8}\text{Fe}_{0.2}\text{O}_x$, [(c) and (d)] $\text{BiVO}_4/\text{Co}_{0.4}\text{Fe}_{0.1}\text{Ce}_{0.5}\text{O}_x$, and [(e) and (f)] $\text{BiVO}_4/\text{Co}_{0.4}\text{Fe}_{0.1}\text{Ce}_{0.5}\text{O}_x/\text{Ni}_{0.8}\text{Fe}_{0.2}\text{O}_x$.⁵⁴ Reproduced with permission from Liu *et al.*, “Interface engineering for light-driven water oxidation: Unravelling the passivating and catalytic mechanism in BiVO_4 overlayers,” *Sustainable Energy Fuels* 3(1), 127–135 (2019). Copyright 2019 Royal Society of Chemistry.

D. Liquid AFM for *in situ* morphology and electrochemical measurements

Solar fuel devices operating in liquid environments involve active generation and transport of electrons, ions, and gaseous

products. Most AFM techniques typically operate in air or vacuum, whereas EC-AFM techniques allow direct investigation of the sample surface under operating conditions. A number of EC-AFM techniques have recently been demonstrated *in situ* under operating conditions in liquid electrolytes with potential control of the

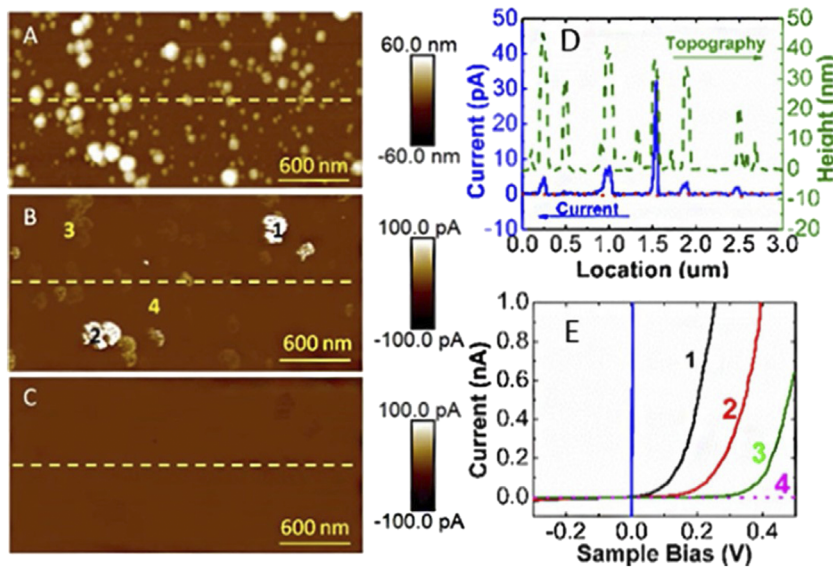


FIG. 9. C-AFM and current–voltage (I – V) relationship of electrolessly deposited Pt on p-Si in air. (a) Topography and [(b) and (c)] current map at biases of (b) 0.3 V and (c) –0.3 V. (d) Cross sectional height (green) and current (blue) corresponding to the dashed yellow line in (a) and (b). (e) I – V characteristics at specific points labeled in (b). The blue curve is an I – V measurement of a Pt thin film deposited onto p-Si via electron-beam evaporation. Nanoparticles are present for positions 1–3, while the substrate is measured at position 4.³² Reproduced with permission from Jiang *et al.*, “Nanoelectrical and nanoelectrochemical imaging of Pt/p-Si and Pt/p+Si electrodes,” *ChemSusChem* 10(22), 4657–4663 (2017). Copyright 2017 Wiley-VCH Verlag GmbH & Co.

substrate and/or the AFM tip. Traditional electrochemical AFM experiments use commercially available, non-conductive AFM tips for liquid-based topography measurements, enabling real-time observations of nanoscale structural changes in the substrate in response to the applied potential. For example, Toma *et al.* studied the *in situ* corrosion of BiVO_4 using EC-AFM and revealed the dissolution of the polycrystalline thin film, which started at exposed facets of grains.⁶⁶

Many transition-metal oxide OER catalysts (NiO_x , CoO_x , etc.) undergo substantial structural changes under operating OER conditions.⁶⁴ The macroscopic electrochemistry and some key characteristics of these processes have been well characterized, but a detailed and comprehensive understanding of the associated structural dynamics would be beneficial. Using EC-AFM, the Boettcher group revealed such structural dynamics by characterizing the morphological evolutions of a series of OER catalysts under varied potentials [Fig. 10(a)].^{63,64} A series of single-layered transition-metal oxy-hydroxides (NiO_xH_y or CoO_xH_y) were synthesized with a well-defined 2D structure and were, subsequently, deposited over flat HOPG conductive substrates. Liquid EC-AFM experiments showed that the MO_xH_y nanosheets grew thicker and rougher as they transitioned from the hydroxide to the oxy-hydroxide under extended voltammetric cycling at potentials that allowed the OER to proceed. The pure NiO_xH_y nanosheet broke into smaller nanoparticles, whereas the mechanical integrity of the

CoO_xH_y or $\text{Ni}_{0.2}\text{Co}_{0.8}\text{O}_x\text{H}_y$ was preserved under analogous conditions [Fig. 10(b)]. These smaller nanoparticles were also found on areas far from the original nanosheet, due to repeated dissolution and redeposition. Continuous voltammetric cycling led to consistent increases in volume, surface area, and redox capacity of the NiO_xH_y sheets. Fe^{3+} cations adsorbed and integrated heterogeneously into the nanosheets as functions of applied potential, further increasing the volume of the nanosheet [Fig. 10(c)]. By use of EC-AFM, the changes in volume and surface area were quantitatively characterized via direct morphological measurements [Fig. 10(d)]. These results showed that the conversion of Ni(OH)_2 into NiOOH changed the nanoscale morphology of the OER catalyst and had an important impact on the mechanical properties of the catalysts.

In addition to the investigation of OER catalysts, the morphological evolution of CO_2 -reduction (CO_2R) catalysts has been observed using *operando* measurements. Grosse *et al.*⁶⁵ showed that immersion of a carbon electrode containing Cu nanocube catalyst particles in an electrolyte while reducing CO_2 led to roughening of the Cu nanocube surface, to the formation of pores, and to a low yield of multi-carbon products. These dynamic structural evolutions were later combined with comprehensive surface analysis to explore the effect on selectivity in CO_2 reduction.⁶⁵

In contrast to the normal three-electrode EC-AFM, AFM-based scanning electrochemical microscopy (SECM-AFM) involves a four-electrode setup with both the sample and the AFM tip

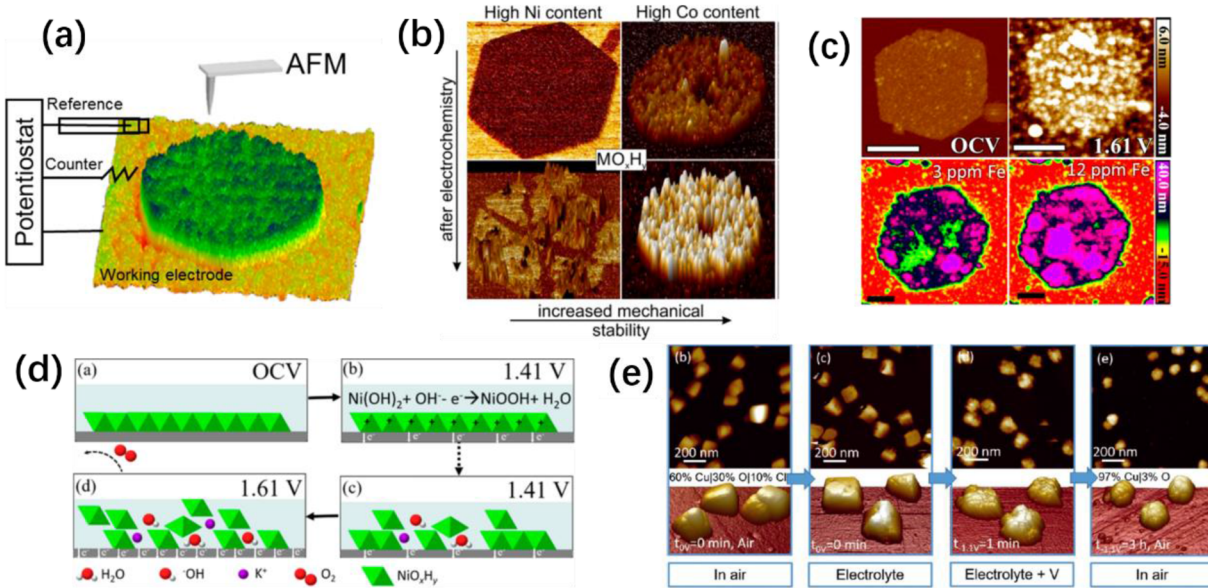


FIG. 10. (a) Schematic illustration of electrochemical AFM (EC-AFM) for morphological investigation;⁶³ (b) comparison of surface morphology of NiO_xH_y and CoO_xH_y nanosheets before and after electrochemistry under OER conditions;⁶⁴ (c) comparison of morphological evolutions of the NiO_xH_y nanosheet from open-circuit to the OER potentials in both Fe-free and Fe-containing electrolytes; (d) schematic illustration of structural transformation of the NiO_xH_y nanosheet under OER potentials; (e) *operando* investigation of morphological evolution of Cu nanocubes under electrochemical CO_2 -reduction conditions.⁶⁵ [(a), (c), and (d)] are reproduced with permission from Deng *et al.*, "Morphology dynamics of single-layered $\text{Ni(OH)}_2/\text{NiOOH}$ nanosheets and subsequent Fe incorporation studied by *in situ* electrochemical atomic force microscopy," *Nano Lett.* **17**(11), 6922–6926 (2017). Copyright 2017 American Chemical Society; (b) is reproduced with permission from Dette *et al.*, "Structural evolution of metal (oxy)hydroxide nanosheets during the oxygen evolution reaction," *ACS Appl. Mater. Interfaces* **11**(6), 5590–5594 (2019). Copyright 2019 American Chemical Society; (e) is reproduced with permission from Grosse *et al.*, "Dynamic changes in the structure, chemical state and catalytic selectivity of Cu nanocubes during CO_2 electroreduction: Size and support effects," *Angew. Chem., Int. Ed.* **57**(21), 6192–6197 (2018). Copyright 2018 Wiley-VCH Verlag GmbH & Co.

acting as independent working electrodes, along with the counter and reference electrodes. Local EC activity over the substrate can be resolved with nanometer resolution by choosing the appropriate redox couples. Nellist *et al.* studied a system involving a Ru(NH₃)₆^{3+/2+} redox couple in the electrolyte over a sample of a metal nanomesh on an insulating substrate.⁴⁰ When the metal was held at a potential that reduces Ru(NH₃)₆³⁺ in the electrolyte, the tip showed higher currents for the oxidation of Ru(NH₃)₆²⁺ over the metal areas than over the insulating areas. Similarly, Jiang *et al.* used SECM-AFM to examine the EC behavior of electrolessly deposited Pt nanoparticles on *p*-Si in an electrolyte.³² Consistent with results from C-AFM in air, only a portion of the Pt nanoparticles displayed substantial EC activity for the reduction of Ru(NH₃)₆³⁺, and the highest current regions were concentrated on only a few Pt particles.

In addition to morphological and SECM investigations, potential-sensing electrochemical AFM (PS-EC-AFM) uses the mostly insulated SECM-AFM probe to directly measure the electrochemical potential of a sample surface when in contact with an electrolyte [Fig. 11(a)]. For potential-sensing, the SECM-AFM probe is used as a fourth electrode, with only the small Pt tip of the AFM probe exposed to the electrolyte, while the rest of the tip and cantilever are well insulated (Fig. 1). In the EC cell shown in Fig. 11(b),

the AFM tip functions as a nanosized electrical probe to measure the EC potential of the surface when the tip is in contact with the sample.^{41,42} The SECM-AFM probe can be used to measure the potential at the front surface (V_{tip}) of an electrode while applying a potential (V_{sub}) to the back-side of the electrode, Fig. 1. For a CoPi OER catalyst on In-doped SnO₂ (ITO), PS-AFM identified that for applied potentials, $V_{\text{sub}} < 0.27$ V vs $E(\text{O}_2/\text{OH}^-)$, the potential of the CoPi did not change; however, at more positive potentials, the CoPi became conductive, and the potential of the front electrode surface tracked the potential applied to the back electrode surface [Fig. 11(c)]. This setup is particularly useful for studying semiconductor surfaces under illumination and for revealing the differences in electrochemical potentials between the front surface and the back contact.^{41,42} For the *n*-Fe₂O₃/CoPi electrode under illumination, the transition from nonconducting to conducting behavior occurred at $V_{\text{sub}} = -0.33$ V vs $E(\text{O}_2/\text{OH}^-)$; moreover, the $V_{\text{tip}} - V_{\text{sub}}$ difference was consistent with the photovoltage produced from the semiconductor.⁴¹

Figure 11(d) shows that for CoPi, the catalytic current was at the same electrochemical potential on either conductive FTO or semiconducting BiVO₄ substrates. This behavior suggests that CoPi acts as both a hole collector and an OER catalyst for the integrated BiVO₄/CoPi photoanode.⁴² In contrast to the macroscopic

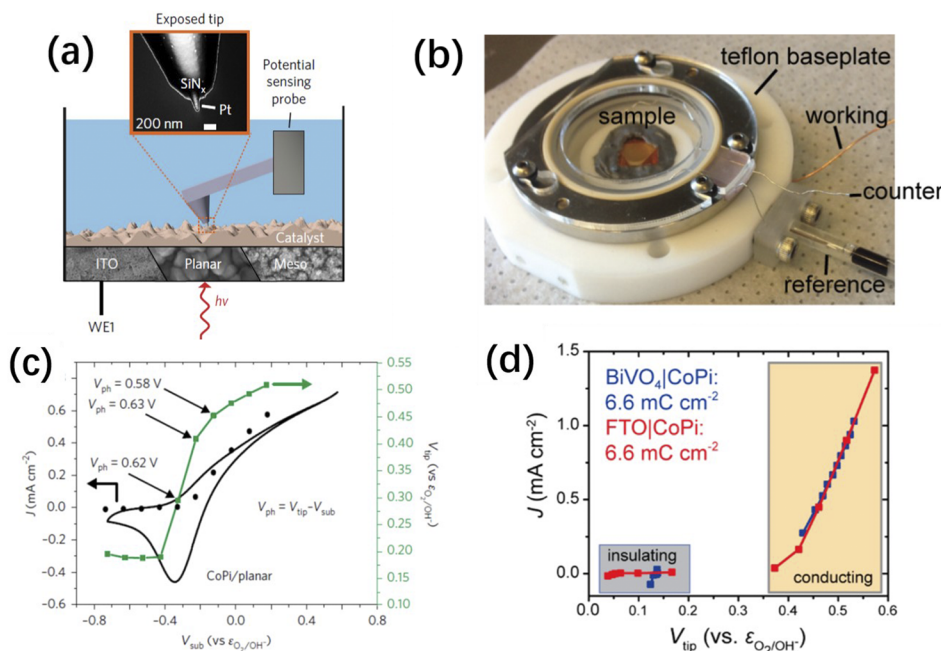


FIG. 11. (a) Schematic illustration of PS-EC-AFM probing the surface potentials of a *n*-Fe₂O₃/CoPi photoelectrode; inset: the fabricated AFM tip used for the potential-sensing (SECM) experiments; (b) an optical image of the custom EC cell used for the PS-EC-AFM experiment, where the Fe₂O₃/CoPi photoelectrode was embedded at the center of the cell; (c) the measured potential of CoPi on planar hematite under illumination.⁴¹ The V_{tip} (green squares) represent the catalyst potential measured by the AFM tip. The simultaneously measured steady-state photocurrent is depicted with black circles, where V_{sub} is the potential applied to the back contact. The black lines are voltammograms collected for the system; (d) comparison of the current density (J) passed and the CoPi surface potential (V_{tip}) measured via the nanoelectrode probe for BiVO₄/CoPi (blue) under illumination and FTO/CoPi (red) in the dark.⁴² (a)-(c) are reproduced with permission from Nellist *et al.*, “Potential-sensing electrochemical atomic force microscopy for *in operando* analysis of water-splitting catalysts and interfaces,” Nat. Energy 3(1), 46–52 (2017). Copyright 2017 Nature Publishing Group; (d) is reproduced with permission from Nellist *et al.*, “Potential-sensing electrochemical AFM shows CoPi as a hole collector and oxygen evolution catalyst on BiVO₄ water-splitting photoanodes,” ACS Energy Lett. 3(9), 2286–2291 (2018). Copyright 2018 American Chemical Society.

dual-working electrode (DWE) technique, PS-AFM can spatially resolve the surface electrochemical potential over the entire electrode surface with nanometer resolution.^{37,67–69} Leveraging the capability of nanometer resolution, PS-AFM has been used to investigate Ni nanoparticles on *n*-Si photoanode surfaces. The open-circuit potentials (E_{oc}) measured at each Ni nanoparticle correlated with their particle size, and a pinch-off phenomenon was revealed through quantitative analysis and modeling.³⁸

III. PERSPECTIVE AND OUTLOOK

Solar fuel research has rapidly evolved in recent years. Disparate PEC components, such as semiconductors, membranes, and catalysts, have been studied in detail, both separately and integrated into operational subsystems. This has allowed significant progress toward the design of a monolithic device that can split water with 19% efficiency.⁷⁰ The development of earth-abundant materials, protective coatings (e.g., TiO₂, NiO_x, CoO_x), and catalysts (e.g. NiMo, NiFeOOH), all stable in corrosive electrolytes, has extended the lifetime of photoelectrodes and leads to a device that could be cost-effective at scale.^{9,71–74} Better understanding of CO₂ reduction catalysts has enabled higher faradaic efficiencies toward hydrocarbon products and the development of a monolithic PEC device that converts CO₂ to formate with 10% efficiency.^{75,76} Despite such progress, key issues such as stability of PEC devices remain. For example, the protected, monolithic III–V tandem devices used to obtain record efficiencies for unassisted water splitting lose performance within the first hour of testing in corrosive electrolytes.⁷⁰ Hence, nanoscale characterization techniques such as AFM are needed to correlate structure–property relationships and provide insight into the macroscopic results. The recent integration of illumination sources and AFMs has greatly expanded the toolkit available for characterizing materials for PEC. Whereas techniques such as SR-SPS and C-AFM are useful to study material properties *ex situ*, emerging liquid AFM developments such as EC-AFM, PS-AFM, and SECM-AFM provide *in situ* characterization of integrated electrodes for solar fuels and leave a wide space for further innovation.

A. AFM in ambient or gaseous environments

SR-SPS measures the local SPV response under illumination and provides insight into both the direction of band bending and the driving force for charge separation. In addition to steady-state measurements, chopped illumination can be used to characterize transient behavior relating to carrier dynamics in light and dark. Importantly, co-catalysts have been demonstrated to enhance the built-in electric field for extracting charge carriers. The formation of asymmetric band bending within a semiconductor crystal by strategic placement of two catalysts can optimize the charge-separation efficiency.

C-AFM can measure the local (photo)current under bias as well as the junction energetics at semiconductor/catalyst interfaces. Probing the morphology-dependent behavior of polycrystalline semiconductors such as α -Fe₂O₃ and BiVO₄ showed that the current was limited at the grain boundaries for α -Fe₂O₃ but not for BiVO₄. Understanding these structure–property relationships

enables the design of crystals optimized for a desired property. C-AFM can locally probe the *I*–*V* characteristics at each pixel of a current map and, subsequently, provide insight into the underlying charge-transfer pathways between electrocatalysts and semiconductors. C-AFM can also provide insight into local failure mechanisms of protective coatings.

Both KPFM and C-AFM have been commonly used under dry or ambient air conditions; however, surface adsorption of gaseous species can alter the junction properties between semiconductors and electrocatalysts. For instance, the barrier heights between various semiconductors and noble metals (Pt/Ru/Rh) change substantially in the presence of H₂,⁷⁷ and the surface work function and electrical behavior of BiVO₄ are sensitive to the ambient atmosphere (N₂/O₂/H₂O).⁷⁸ Thus, the effects of gas adsorption on samples that operate in specific atmospheres need to be elucidated. For example, *operando* AFM studies of earth-abundant HER, CO₂R, and OER catalysts should consider the effects of the generation and adsorption of reactants or products on the electrode.^{79–81} Moreover, the properties at the triple-phase boundary (TPB), the intersection of the (photo)catalyst, membrane, and vapor, control device performance for the vapor-fed systems being considered for solar CO₂ conversion systems.^{82–84} Under controlled vapor-feed conditions, the AFM-based techniques have the potential to probe nanoscale changes in morphology and electrical properties at these TPBs.

B. *Operando* liquid AFM

Liquid-based *operando* AFM techniques measure changes in surface morphology, surface potential, adhesion of nanoparticles, and reactivity of catalyst or protective coatings. These liquid-based AFM techniques offer insight into differences in reactivity of the sample between dry and wet/ionic environments and can probe changes in the sample under applied potentials and electrolytes. PS-AFM, or C-AFM using SECM tips, allows the spatial resolution of local EC activity correlated with the sample topography and composition (Fig. 1). PS-AFM allows understanding of the electrochemical potential on the surface of an electrode, the photovoltage generated by a photoelectrode, and anisotropic distribution of the potential on heterogeneous electrodes as well as at semiconductor/catalyst interfaces. C-AFM and SR-SPS have been used to measure the anisotropic charge migration to different facets of a single crystal in air. PS-AFM can extend this method to *operando* measurements under liquid and with an applied potential, to understand the differences in chemical reactivity at grain boundaries, crystal faults, and different crystal facets.

The KPFM technique has been used in both polar and non-polar solvents to understand various surface phenomena such as adsorption and the electrical double layer.^{85–87} However, due to screening by the electrolyte, the use of KPFM is difficult under the electrolyte concentrations normally used in electrochemistry. A comprehensive review of the use of KPFM under liquids has been recently presented.⁸⁸

Solar fuel systems are often operated in strongly acidic or alkaline environments, presenting substantial stability challenges to all component materials. The development of SECM-AFM cantilevers that are stable in these environments is needed. An understanding

of the stability and corrosion mechanisms of semiconductors, catalysts, and protection layers is currently incomplete for many PEC materials.⁸⁹ The use of AFM techniques in liquids allows for direct visualization of these morphological changes and corrosion processes of solar fuel materials over time.⁶⁶ For example, the corrosion of protection layers can occur through nanosized pinholes present in the film.^{62,90} Thus, the development of *operando* AFM techniques to characterize pinholes is needed to better understand their formation mechanism and impact in solar fuel devices.

The fabrication of photoelectrodes with new semiconductors is often hindered by the difficulties of synthesizing high quality, macroscopic single crystals. The ease of synthesis and scalability of solution-processible particulate semiconductor photocatalysts makes these materials attractive options, but nanoparticles often yield low efficiencies and overall performance.⁹¹ PS-AFM offers new opportunities for studying the structure–property relations of these more processible semiconductor particulate systems to better guide semiconductor fabrication. Under controlled illumination, PS-AFM can characterize the photo-potential generation, whereas SECM-AFM can spatially map out PEC activities over micron-sized semiconductor particles in electrolyte and under potential control.^{92,93}

AUTHORS' CONTRIBUTIONS

W.Y. and H.J.F. contributed equally to this work.

ACKNOWLEDGMENTS

This material is based upon work performed by the Joint Center for Artificial Photosynthesis, a DOE Energy Innovation Hub, supported through the Office of Science of the U.S. Department of Energy under Award No. DE-SC0004993. The authors would like to thank the Beckman Institute at the California Institute of Technology for continuous support.

DATA AVAILABILITY

The data that support the findings of this study are available within the article.

REFERENCES

- ¹M. G. Walter, E. L. Warren, J. R. McKone, S. W. Boettcher, Q. Mi, E. A. Santori, and N. S. Lewis, “Solar water splitting cells,” *Chem. Rev.* **110**(11), 6446–6473 (2010).
- ²N. S. Lewis, “Research opportunities to advance solar energy utilization,” *Science* **351**(6271), aad1920 (2016).
- ³S. Chabi, K. M. Papadantonakis, N. S. Lewis, and M. S. Freund, “Membranes for artificial photosynthesis,” *Energy Environ. Sci.* **10**(6), 1320–1338 (2017).
- ⁴J. R. McKone, N. S. Lewis, and H. B. Gray, “Will solar-driven water-splitting devices see the light of day?,” *Chem. Mater.* **26**(1), 407–414 (2014).
- ⁵G. Katsouris and H. Frei, “Ultrathin oxide layers for nanoscale integration of molecular light absorbers, catalysts, and complete artificial photosystems,” *J. Chem. Phys.* **150**(4), 041501 (2019).
- ⁶J. M. Spurgeon, M. G. Walter, J. Zhou, P. A. Kohl, and N. S. Lewis, “Electrical conductivity, ionic conductivity, optical absorption, and gas separation properties of ionically conductive polymer membranes embedded with Si microwire arrays,” *Energy Environ. Sci.* **4**(5), 1772 (2011).
- ⁷S. Haussener, C. Xiang, J. M. Spurgeon, S. Ardo, N. S. Lewis, and A. Z. Weber, “Modeling, simulation, and design criteria for photoelectrochemical water-splitting systems,” *Energy Environ. Sci.* **5**(12), 9922 (2012).
- ⁸E. Verlage, S. Hu, R. Liu, R. J. R. Jones, K. Sun, C. Xiang, N. S. Lewis, and H. A. Atwater, “A monolithically integrated, intrinsically safe, 10% efficient, solar-driven water-splitting system based on active, stable earth-abundant electrocatalysts in conjunction with tandem III-V light absorbers protected by amorphous TiO₂ films,” *Energy Environ. Sci.* **8**(11), 3166–3172 (2015).
- ⁹D. Bae, B. Seger, P. C. K. Vesborg, O. Hansen, and I. Chorkendorff, “Strategies for stable water splitting via protected photoelectrodes,” *Chem. Soc. Rev.* **46**(7), 1933–1954 (2017).
- ¹⁰J. Zhu, F. Fan, R. Chen, H. An, Z. Feng, and C. Li, “Direct imaging of highly anisotropic photogenerated charge separations on different facets of a single BiVO₄ photocatalyst,” *Angew. Chem., Int. Ed.* **54**(31), 9111–9114 (2015).
- ¹¹S. C. Warren, K. Voitchovsky, H. Dotan, C. M. Leroy, M. Cornuz, F. Stellacci, C. Hébert, A. Rothschild, and M. Grätzel, “Identifying champion nanostructures for solar water-splitting,” *Nat. Mater.* **12**(9), 842–849 (2013).
- ¹²E. L. Warren, H. A. Atwater, and N. S. Lewis, “Silicon microwire arrays for solar energy-conversion applications,” *J. Phys. Chem. C* **118**(2), 747–759 (2014).
- ¹³D. M. Fabian, S. Hu, N. Singh, F. A. Houle, T. Hisatomi, K. Domen, F. E. Osterloh, and S. Ardo, “Particle suspension reactors and materials for solar-driven water splitting,” *Energy Environ. Sci.* **8**(10), 2825–2850 (2015).
- ¹⁴S. Yalamanchili, H. S. Emmer, K. T. Fountaine, C. T. Chen, N. S. Lewis, and H. A. Atwater, “Enhanced absorption and <1% spectrum-and-angle-averaged reflection in tapered microwire arrays,” *ACS Photonics* **3**(10), 1854–1861 (2016).
- ¹⁵P. A. Kempler, M. A. Gonzalez, K. M. Papadantonakis, and N. S. Lewis, “Hydrogen evolution with minimal parasitic light absorption by dense Co-P catalyst films on structured p-Si photocathodes,” *ACS Energy Lett.* **3**, 612–617 (2018).
- ¹⁶M. R. Shaner, J. R. McKone, H. B. Gray, and N. S. Lewis, “Functional integration of Ni–Mo electrocatalysts with Si microwire array photocathodes to simultaneously achieve high fill factors and light-limited photocurrent densities for solar-driven hydrogen evolution,” *Energy Environ. Sci.* **8**(10), 2977–2984 (2015).
- ¹⁷H. Sun, Z. Ma, Y. Qiu, H. Liu, and G. Gao, “Ni@NiO nanowires on nickel foam prepared via “acid hungry” strategy: High supercapacitor performance and robust electrocatalysts for water splitting reaction,” *Small* **14**(31), 1800294 (2018).
- ¹⁸R. C. Rossi, M. X. Tan, and N. S. Lewis, “Size-dependent electrical behavior of spatially inhomogeneous barrier height regions on silicon,” *Appl. Phys. Lett.* **77**(17), 2698–2700 (2000).
- ¹⁹Z. Huang, J. Jiang, Y. Hua, C. Li, M. Wagner, H. J. Lewerenz, M. P. Soriaga, and C. Anfuso, “Atomic force microscopy for solar fuels research: An introductory review,” *Energy Environ. Focus* **4**(4), 260–277 (2015).
- ²⁰G. Binnig, C. F. Quate, and C. Gerber, “Atomic force microscope,” *Phys. Rev. Lett.* **56**(9), 930–933 (1986).
- ²¹R. Giridharagopal, J. T. Precht, S. Jariwala, L. Collins, S. Jesse, S. V. Kalinin, and D. S. Ginger, “Time-resolved electrical scanning probe microscopy of layered perovskites reveals spatial variations in photoinduced ionic and electronic carrier motion,” *ACS Nano* **13**(3), 2812–2821 (2019).
- ²²J. Kong, R. Giridharagopal, J. S. Harrison, and D. S. Ginger, “Identifying nanoscale structure–function relationships using multimodal atomic force microscopy, dimensionality reduction, and regression techniques,” *J. Phys. Chem. Lett.* **9**(12), 3307–3314 (2018).
- ²³D. C. Coffey, O. G. Reid, D. B. Rodovsky, G. P. Bartholomew, and D. S. Ginger, “Mapping local photocurrents in polymer/fullerene solar cells with photoconductive atomic force microscopy,” *Nano Lett.* **7**(3), 738–744 (2007).
- ²⁴P. A. Cox, M. S. Glaz, J. S. Harrison, S. R. Peurifoy, D. C. Coffey, and D. S. Ginger, “Imaging charge transfer state excitations in polymer/fullerene solar cells with time-resolved electrostatic force microscopy,” *J. Phys. Chem. Lett.* **6**(15), 2852–2858 (2015).
- ²⁵L. S. C. Pingree, O. G. Reid, and D. S. Ginger, “Electrical scanning probe microscopy on active organic electronic devices,” *Adv. Mater.* **21**(1), 19–28 (2009).

- ²⁶Y. Almadori, D. Moerman, J. L. Martinez, P. Leclère, and B. Grévin, "Multi-modal noncontact atomic force microscopy and Kelvin probe force microscopy investigations of organolead tribromide perovskite single crystals," *Beilstein J. Nanotechnol.* **9**, 1695–1704 (2018).
- ²⁷P. Schön, K. Bagdi, K. Molnár, P. Markus, B. Pukánszky, and G. J. Vancso, "Quantitative mapping of elastic moduli at the nanoscale in phase separated polyurethanes by AFM," *Eur. Polym. J.* **47**(4), 692–698 (2011).
- ²⁸J. Adamcik, A. Berquand, and R. Mezzenga, "Single-step direct measurement of amyloid fibrils stiffness by peak force quantitative nanomechanical atomic force microscopy," *Appl. Phys. Lett.* **98**(19), 193701 (2011).
- ²⁹F. Rico, C. Su, and S. Scheuring, "Mechanical mapping of single membrane proteins at submolecular resolution," *Nano Lett.* **11**(9), 3983–3986 (2011).
- ³⁰B. Pittenger, N. Erina, and C. Su, "Quantitative Mechanical Property Mapping at the Nanoscale with PeakForce QNM; Application Note #128," (Bruker Nano Surface Division, 2010), pp. 1–12.
- ³¹Q. Zhong, D. Inniss, K. Kjoller, and V. B. Elings, "Fractured polymer/silica fiber surface studied by tapping mode atomic force microscopy," *Surf. Sci. Lett.* **290**(1–2), L688–L692 (1993).
- ³²J. Jiang, Z. Huang, C. Xiang, R. Poddar, H.-J. Lewerenz, K. M. Papadantonakis, N. S. Lewis, and B. S. Brunschwig, "Nanoelectrical and nanoelectrochemical imaging of Pt/p-Si and Pt/p⁺-Si electrodes," *ChemSusChem* **10**(22), 4657–4663 (2017).
- ³³L. Letertre, R. Roche, O. Douhéret, H. G. Kassa, D. Mariolle, N. Chevalier, L. Borowik, P. Dumas, B. Grévin, R. Lazzaroni, and P. Leclère, "A scanning probe microscopy study of nanostructured TiO₂/poly(3-hexylthiophene) hybrid heterojunctions for photovoltaic applications," *Beilstein J. Nanotechnol.* **9**, 2087–2096 (2018).
- ³⁴L. Letertre, O. Douhéret, M. Bougouma, T. Doneux, R. Lazzaroni, C. Buess-Herman, and P. Leclère, "Nanoscale study of MoSe₂/poly(3-hexylthiophene) bulk heterojunctions for hybrid photovoltaic applications," *Sol. Energy Mater. Sol. Cells* **145**, 116–125 (2016).
- ³⁵B. Grévin, P.-O. Schwartz, L. Biniek, M. Brinkmann, N. Leclerc, E. Zaborova, and S. Méry, "High-resolution noncontact AFM and Kelvin probe force microscopy investigations of self-assembled photovoltaic donor–acceptor dyads," *Beilstein J. Nanotechnol.* **7**, 799–808 (2016).
- ³⁶W. Melitz, J. Shen, A. C. Kummel, and S. Lee, "Kelvin probe force microscopy and its application," *Surf. Sci. Rep.* **66**(1), 1–27 (2011).
- ³⁷F. Lin and S. W. Boettcher, "Adaptive semiconductor/electrocatalyst junctions in water-splitting photoanodes," *Nat. Mater.* **13**(1), 81–86 (2014).
- ³⁸F. A. L. Laskowski, S. Z. Oener, M. R. Nellist, A. M. Gordon, D. C. Bain, J. L. Fehrs, and S. W. Boettcher, "Nanoscale semiconductor/catalyst interfaces in photoelectrochemistry," *Nat. Mater.* **19**, 69–76 (2020).
- ³⁹I. V. Pobelov, M. Mohos, K. Yoshida, V. Kolivoska, A. Avdic, A. Lugstein, E. Bertagnolli, K. Leonhardt, G. Denuault, B. Gollas, and T. Wandlowski, "Electrochemical current-sensing atomic force microscopy in conductive solutions," *Nanotechnology* **24**(11), 115501 (2013).
- ⁴⁰M. R. Nellist, Y. Chen, A. Mark, S. Gödrich, C. Stelling, J. Jiang, R. Poddar, C. Li, R. Kumar, G. Papastavrou, M. Retsch, B. S. Brunschwig, Z. Huang, C. Xiang, and S. W. Boettcher, "Atomic force microscopy with nanoelectrode tips for high resolution electrochemical, nanoadhesion and nanoelectrical imaging," *Nanotechnology* **28**(9), 095711 (2017).
- ⁴¹M. R. Nellist, F. A. L. Laskowski, J. Qiu, H. Hajibabaei, K. Sivula, T. W. Hamann, and S. W. Boettcher, "Potential-sensing electrochemical atomic force microscopy for *in operando* analysis of water-splitting catalysts and interfaces," *Nat. Energy* **3**(1), 46–52 (2017).
- ⁴²M. R. Nellist, J. Qiu, F. A. L. Laskowski, F. M. Toma, and S. W. Boettcher, "Potential-sensing electrochemical AFM shows CoPi as a hole collector and oxygen evolution catalyst on BiVO₄ water-splitting photoanodes," *ACS Energy Lett.* **3**(9), 2286–2291 (2018).
- ⁴³J. Eichhorn, C. Kastl, J. K. Cooper, D. Ziegler, A. M. Schwartzberg, I. D. Sharp, and F. M. Toma, "Nanoscale imaging of charge carrier transport in water splitting photoanodes," *Nat. Commun.* **9**(1), 2597 (2018).
- ⁴⁴R. Chen, F. Fan, T. Dittrich, and C. Li, "Imaging photogenerated charge carriers on surfaces and interfaces of photocatalysts with surface photovoltaic microscopy," *Chem. Soc. Rev.* **47**(22), 8238–8262 (2018).
- ⁴⁵R. Chen, S. Pang, H. An, J. Zhu, S. Ye, Y. Gao, F. Fan, and C. Li, "Charge separation via asymmetric illumination in photocatalytic Cu₂O particles," *Nat. Energy* **3**(8), 655–663 (2018).
- ⁴⁶H. Wang, X. Wang, R. Chen, H. Zhang, X. Wang, J. Wang, J. Zhang, L. Mu, K. Wu, F. Fan, X. Zong, and C. Li, "Promoting photocatalytic H₂ evolution on organic–inorganic hybrid perovskite nanocrystals by simultaneous dual-charge transportation modulation," *ACS Energy Lett.* **4**(1), 40–47 (2019).
- ⁴⁷Z. Schumacher, Y. Miyahara, A. Spielhofer, and P. Grutter, "Measurement of surface photovoltage by atomic force microscopy under pulsed illumination," *Phys. Rev. Appl.* **5**(4), 044018 (2016).
- ⁴⁸Y. Gao, J. Zhu, H. An, P. Yan, B. Huang, R. Chen, F. Fan, and C. Li, "Directly probing charge separation at interface of TiO₂ phase junction," *J. Phys. Chem. Lett.* **8**(7), 1419–1423 (2017).
- ⁴⁹R. Chen, J. Zhu, H. An, F. Fan, and C. Li, "Unravelling charge separation via surface built-in electric fields within single particulate photocatalysts," *Faraday Discuss.* **198**, 473–479 (2017).
- ⁵⁰D. Li, Y. Liu, W. Shi, C. Shao, S. Wang, C. Ding, T. Liu, F. Fan, J. Shi, and C. Li, "Crystallographic-orientation-dependent charge separation of BiVO₄ for solar water oxidation," *ACS Energy Lett.* **4**(4), 825–831 (2019).
- ⁵¹J. Zhu, S. Pang, T. Dittrich, Y. Gao, W. Nie, J. Cui, R. Chen, H. An, F. Fan, and C. Li, "Visualizing the nano cocatalyst aligned electric fields on single photocatalyst particles," *Nano Lett.* **17**(11), 6735–6741 (2017).
- ⁵²L. Kronik, "Surface photovoltage phenomena: Theory, experiment, and applications," *Surf. Sci. Rep.* **37**(1–5), 1–206 (1999).
- ⁵³R. Chen, S. Pang, H. An, T. Dittrich, F. Fan, and C. Li, "Giant defect-induced effects on nanoscale charge separation in semiconductor photocatalysts," *Nano Lett.* **19**(1), 426–432 (2019).
- ⁵⁴G. Liu, J. Eichhorn, C.-M. Jiang, M. C. Scott, L. H. Hess, J. M. Gregoire, J. A. Haber, I. D. Sharp, and F. M. Toma, "Interface engineering for light-driven water oxidation: Unravelling the passivating and catalytic mechanism in BiVO₄ overlayers," *Sustainable Energy Fuels* **3**(1), 127–135 (2019).
- ⁵⁵Y. Yu, C. Sun, X. Yin, J. Li, S. Cao, C. Zhang, P. M. Voyles, and X. Wang, "Metastable intermediates in amorphous titanium oxide: A hidden role leading to ultra-stable photoanode protection," *Nano Lett.* **18**(8), 5335–5342 (2018).
- ⁵⁶C. H. Seager and D. S. Ginley, "Passivation of grain boundaries in polycrystalline silicon," *Appl. Phys. Lett.* **34**(5), 337–340 (1979).
- ⁵⁷M. Rezeq, K. Eledlebi, M. Ismail, R. K. Dey, and B. Cui, "Theoretical and experimental investigations of nano-Schottky contacts," *J. Appl. Phys.* **120**(4), 044302 (2016).
- ⁵⁸R. W. Carpick, D. F. Ogletree, and M. Salmeron, "A general equation for fitting contact area and friction vs load measurements," *J. Colloid Interface Sci.* **211**(2), 395–400 (1999).
- ⁵⁹J. R. McKone, E. L. Warren, M. J. Bierman, S. W. Boettcher, B. S. Brunschwig, N. S. Lewis, and H. B. Gray, "Evaluation of Pt, Ni, and Ni–Mo electrocatalysts for hydrogen evolution on crystalline Si electrodes," *Energy Environ. Sci.* **4**(9), 3573 (2011).
- ⁶⁰A. R. Zeradjanin, A. A. Topalov, Q. Van Overmeire, S. Cherevko, X. Chen, E. Ventosa, W. Schuhmann, and K. J. J. Mayrhofer, "Rational design of the electrode morphology for oxygen evolution—Enhancing the performance for catalytic water oxidation," *RSC Adv.* **4**(19), 9579 (2014).
- ⁶¹P. Nunez, M. H. Richter, B. D. Piercy, C. W. Roske, M. Cabán-Acevedo, M. D. Losego, S. J. Konezny, D. J. Fermin, S. Hu, B. S. Brunschwig, and N. S. Lewis, "Characterization of electronic transport through amorphous TiO₂ produced by atomic layer deposition," *J. Phys. Chem. C* **123**(33), 20116–20129 (2019).
- ⁶²S. Hu, M. R. Shaner, J. A. Beardslee, M. Lichberman, B. S. Brunschwig, and N. S. Lewis, "Amorphous TiO₂ coatings stabilize Si, GaAs, and GaP photoanodes for efficient water oxidation," *Science* **344**(6187), 1005 (2014).
- ⁶³J. Deng, M. R. Nellist, M. B. Stevens, C. Dette, Y. Wang, and S. W. Boettcher, "Morphology dynamics of single-layered Ni(OH)₂/NiOOH nanosheets and subsequent Fe incorporation studied by *in situ* electrochemical atomic force microscopy," *Nano Lett.* **17**(11), 6922–6926 (2017).
- ⁶⁴C. Dette, M. R. Hurst, J. Deng, M. R. Nellist, and S. W. Boettcher, "Structural evolution of metal (oxy)hydroxide nanosheets during the oxygen evolution reaction," *ACS Appl. Mater. Interfaces* **11**(6), 5590–5594 (2019).

- ⁶⁵P. Grosse, D. Gao, F. Scholten, I. Sinev, H. Mistry, and B. R. Cuenya, "Dynamic changes in the structure, chemical state and catalytic selectivity of Cu nanocubes during CO₂ electroreduction: Size and support effects," *Angew. Chem., Int. Ed.* **57**(21), 6192–6197 (2018).
- ⁶⁶F. M. Toma, J. K. Cooper, V. Kunzelmann, M. T. McDowell, J. Yu, D. M. Larson, N. J. Borys, C. Abelyan, J. W. Beeman, K. M. Yu, J. Yang, L. Chen, M. R. Shaner, J. Spurgeon, F. A. Houle, K. A. Persson, and I. D. Sharp, "Mechanistic insights into chemical and photochemical transformations of bismuth vanadate photoanodes," *Nat. Commun.* **7**(1), 12012 (2016).
- ⁶⁷F. A. L. Laskowski, M. R. Nellist, R. Venkatkarthick, and S. W. Boettcher, "Junction behavior of n-Si photoanodes protected by thin Ni elucidated from dual working electrode photoelectrochemistry," *Energy Environ. Sci.* **10**(2), 570–579 (2017).
- ⁶⁸J. Qiu, H. Hajibabaei, M. R. Nellist, F. A. L. Laskowski, T. W. Hamann, and S. W. Boettcher, "Direct in situ measurement of charge transfer processes during photoelectrochemical water oxidation on catalyzed hematite," *ACS Cent. Sci.* **3**(9), 1015–1025 (2017).
- ⁶⁹J. Qiu, H. Hajibabaei, M. R. Nellist, F. A. L. Laskowski, S. Z. Oener, T. W. Hamann, and S. W. Boettcher, "Catalyst deposition on photoanodes: The roles of intrinsic catalytic activity, catalyst electrical conductivity, and semiconductor morphology," *ACS Energy Lett.* **3**(4), 961–969 (2018).
- ⁷⁰W.-H. Cheng, M. H. Richter, M. M. May, J. Ohlmann, D. Lackner, F. Dimroth, T. Hannappel, H. A. Atwater, and H.-J. Lewerenz, "Monolithic photoelectrochemical device for direct water splitting with 19% efficiency," *ACS Energy Lett.* **3**(8), 1795–1800 (2018).
- ⁷¹K. Sun, F. H. Saadi, M. F. Lichterman, W. G. Hale, H.-P. Wang, X. Zhou, N. T. Plymale, S. T. Omelchenko, J.-H. He, K. M. Papadantonakis, B. S. Brunschwig, and N. S. Lewis, "Stable solar-driven oxidation of water by semiconducting photoanodes protected by transparent catalytic nickel oxide films," *Proc. Natl. Acad. Sci. U. S. A.* **112**(12), 3612 (2015).
- ⁷²X. Zhou, R. Liu, K. Sun, K. M. Papadantonakis, B. S. Brunschwig, and N. S. Lewis, "570 mV photovoltage, stabilized n-Si/CoO_x heterojunction photoanodes fabricated using atomic layer deposition," *Energy Environ. Sci.* **9**(3), 892–897 (2016).
- ⁷³E. L. Warren, J. R. McKone, H. A. Atwater, H. B. Gray, and N. S. Lewis, "Hydrogen-evolution characteristics of Ni-Mo-coated, radial junction, N⁺p-silicon microwire array photocathodes," *Energy Environ. Sci.* **5**(11), 9653 (2012).
- ⁷⁴L. Trotochaud, S. L. Young, J. K. Ranney, and S. W. Boettcher, "Nickel-iron oxyhydroxide oxygen-evolution electrocatalysts: The role of intentional and incidental iron incorporation," *J. Am. Chem. Soc.* **136**(18), 6744–6753 (2014).
- ⁷⁵Y. Wang, Z. Wang, C.-T. Dinh, J. Li, A. Ozden, M. G. Kibria, A. Seifitokaldani, C.-S. Tan, C. M. Gabardo, M. Luo, H. Zhou, F. Li, Y. Lum, C. McCallum, Y. Xu, M. Liu, A. Proppe, A. Johnston, P. Todorovic, T.-T. Zhuang, D. Sinton, S. O. Kelley, and E. H. Sargent, "Catalyst synthesis under CO₂ electroreduction favours faceting and promotes renewable fuels electrosynthesis," *Nat. Catal.* **3**(2), 98–106 (2020).
- ⁷⁶X. Zhou, R. Liu, K. Sun, Y. Chen, E. Verlage, S. A. Francis, N. S. Lewis, and C. Xiang, "Solar-driven reduction of 1 atm of CO₂ to formate at 10% energy-conversion efficiency by use of a TiO₂-protected III-V tandem photoanode in conjunction with a bipolar membrane and a Pd/C cathode," *ACS Energy Lett.* **1**(4), 764–770 (2016).
- ⁷⁷D. E. Aspnes and A. Heller, "Photoelectrochemical hydrogen evolution and water photolyzing semiconductor suspensions: Properties of platinum group metal catalyst-semiconductor contacts in air and in hydrogen," *J. Phys. Chem.* **87**(24), 4919–4929 (1983).
- ⁷⁸J. Eichhorn, C. Kastl, A. M. Schwartzberg, I. D. Sharp, and F. M. Toma, "Disentangling the role of surface chemical interactions on interfacial charge transport at BiVO₄ photoanodes," *ACS Appl. Mater. Interfaces* **10**(41), 35129–35136 (2018).
- ⁷⁹F. H. Saadi, A. I. Carim, E. Verlage, J. C. Hemminger, N. S. Lewis, and M. P. Soriaga, "CoP as an acid-stable active electrocatalyst for the hydrogen-evolution reaction: Electrochemical synthesis, interfacial characterization and performance evaluation," *J. Phys. Chem. C* **118**(50), 29294–29300 (2014).
- ⁸⁰E. J. Popczun, J. R. McKone, C. G. Read, A. J. Biacchi, A. M. Wiltrot, N. S. Lewis, and R. E. Schaak, "Nanostructured nickel phosphide as an electrocatalyst for the hydrogen evolution reaction," *J. Am. Chem. Soc.* **135**(25), 9267–9270 (2013).
- ⁸¹T. F. Jaramillo, K. P. Jorgensen, J. Bonde, J. H. Nielsen, S. Horch, and I. Chorkendorff, "Identification of active edge sites for electrochemical H₂ evolution from MoS₂ nanocatalysts," *Science* **317**(5834), 100–102 (2007).
- ⁸²D. Higgins, C. Hahn, C. Xiang, T. F. Jaramillo, and A. Z. Weber, "Gas-diffusion electrodes for carbon dioxide reduction: A new paradigm," *ACS Energy Lett.* **4**(1), 317–324 (2019).
- ⁸³W.-H. Cheng, M. H. Richter, I. Sullivan, D. M. Larson, C. Xiang, B. S. Brunschwig, and H. A. Atwater, "CO₂ reduction to CO with 19% efficiency in a solar-driven gas diffusion electrode flow cell under outdoor solar illumination," *ACS Energy Lett.* **5**(2), 470–476 (2020).
- ⁸⁴F. P. G. de Arquer, C.-T. Dinh, A. Ozden, J. Wicks, C. McCallum, A. R. Kirmani, D.-H. Nam, C. Gabardo, A. Seifitokaldani, X. Wang, Y. C. Li, F. Li, J. Edwards, L. J. Richter, S. J. Thorpe, D. Sinton, and E. H. Sargent, "CO₂ electrolysis to multicarbon products at activities greater than 1 A cm⁻²," *Science* **367**(6478), 661–666 (2020).
- ⁸⁵L. Collins, S. Jesse, J. I. Kilpatrick, A. Tselev, M. B. Okatan, S. V. Kalinin, and B. J. Rodriguez, "Kelvin probe force microscopy in liquid using electrochemical force microscopy," *Beilstein J. Nanotechnol.* **6**, 201–214 (2015).
- ⁸⁶L. Collins, S. Jesse, J. I. Kilpatrick, A. Tselev, O. Varenyk, M. B. Okatan, S. A. L. Weber, A. Kumar, N. Balke, S. V. Kalinin, and B. J. Rodriguez, "Probing charge screening dynamics and electrochemical processes at the solid–liquid interface with electrochemical force microscopy," *Nat. Commun.* **5**(1), 3871 (2014).
- ⁸⁷K. Umeda, K. Kobayashi, N. Oyabu, Y. Hirata, K. Matsushige, and H. Yamada, "Practical aspects of Kelvin-probe force microscopy at solid/liquid interfaces in various liquid media," *J. Appl. Phys.* **116**(13), 134307 (2014).
- ⁸⁸L. Collins, J. I. Kilpatrick, S. V. Kalinin, and B. J. Rodriguez, "Towards nanoscale electrical measurements in liquid by advanced KPFM techniques: A review," *Rep. Prog. Phys.* **81**(8), 086101 (2018).
- ⁸⁹W. T. Osowiecki, J. J. Nussbaum, G. A. Kamat, G. Katsoukis, M. Ledendecker, H. Frei, A. T. Bell, and A. P. Alivisatos, "Factors and dynamics of Cu nanocrystal reconstruction under CO₂ reduction," *ACS Appl. Energy Mater.* **2**, 7744–7749 (2019).
- ⁹⁰M. F. Lichterman, K. Sun, S. Hu, X. Zhou, M. T. McDowell, M. R. Shaner, M. H. Richter, E. J. Crumlin, A. I. Carim, F. H. Saadi, B. S. Brunschwig, and N. S. Lewis, "Protection of inorganic semiconductors for sustained, efficient photoelectrochemical water oxidation," *Catal. Today* **262**, 11–23 (2016).
- ⁹¹Q. Wang, M. Nakabayashi, T. Hisatomi, S. Sun, S. Akiyama, Z. Wang, Z. Pan, X. Xiao, T. Watanabe, T. Yamada, N. Shibata, T. Takata, and K. Domen, "Oxysulfide photocatalyst for visible-light-driven overall water splitting," *Nat. Mater.* **18**(8), 827–832 (2019).
- ⁹²L. Wang, M. Schmid, and J. B. Sambur, "Single nanoparticle photoelectrochemistry: What is next?," *J. Chem. Phys.* **151**(18), 180901 (2019).
- ⁹³Y. He, R. Chen, W. Fa, B. Zhang, and D. Wang, "Surface chemistry and photoelectrochemistry—Case study on tantalum nitride," *J. Chem. Phys.* **151**(13), 130902 (2019).